# NOVEL METHODS FOR MULTI-MODAL MR IMAGE ANALYSIS WITH APPLICATIONS TO PARKINSON'S

by

Jingyun Chen

M.Sc., Tsinghua University, 2006

B.Sc., Tsinghua University, 2003

A Thesis submitted in partial fulfillment
of the requirements for the degree of
Doctor of Philosophy
in the
School of Engineering Science
Faculty of Applied Sciences


SIMON FRASER UNIVERSITY
Fall 2011

## APPROVAL

**Name:** Jingyun Chen

**Degree:** Doctor of Philosophy

**Title of Thesis:** Novel methods for multi-modal MR image analysis with applications to Parkinson's

**Examining Committee:** Dr. Ivan Bajic, Associate Professor
Chair

---

Dr. Mirza Faisal Beg, Senior Supervisor
Associate Professor

---

Dr. Martin J. McKeown, Supervisor, Professor
Medicine Department, University of British Columbia

---

Dr. Shawn Stapleton, Supervisor, Professor

---

Dr. Stella Atkins, Internal Examiner
Professor, School of Computing Science

---

Dr. Elizabeth Aylward, External Examiner
Affiliate Professor, Department of Psychology
University of Washington

**Date Approved:** November 28, 2011

# Partial Copyright Licence

# Abstract

Parkinson's Disease (PD) affects approximately 1% of the population above the age of 65.The morphological changes in PD are typically not obvious, even to the trained eyes. Thus computational methods are needed to determine the existence and potential significance of robust changes in brain morphometry in PD. In this thesis we present a number of novel signal and image processing methods, that when applied to different Magnetic Resonance Imaging (MRI) techniques, can be used for the diagnosis and monitoring of PD. We first motivate the research by measuring the extent of residual anatomical variability (RAV) after spatial normalization (Chapter 1). In Chapter 2, we present a novel brain morphometry method, based on the analysis of the deformation field required to map template regions of interest (ROIs) to the corresponding ROIs in the individual brains images to be assessed. Chapter 3 summarizes the development of an algorithm to improve registration of the midbrain region, the primary site of pathology in PD. We also propose a novel method for joint analysis of structural images and diffusion tensor images (DTI) using the Fukunaga-Koontz Transform (FKT), which jointly transforms anatomical and DTI data into the same spatial components, but with complementary loadings (Chapter 4). This allows selection of linear subspaces which are heavily weighted on DTI changes relatively insensitive to residual morphological differences, and vice versa. All the proposed methods have been validated with clinic MRI data of both PD subjects and age-matched normal control subjects. To complement the above studies, we further designed a module-based work flow to extract time courses from function MRI (fMRI) signals, using automated segmentation of structural MRI data as masks (Appendix A). This has facilitated the analysis of fMRI studies in PD, such as examining the compensatory changes seen in PD.

# Acknowledgments

First I would like to thank my senior supervisor Dr. Mirza Faisal Beg for introducing me to the amazing world of neuroimaging, and financially supporting my entire PhD program. I also want to thank Dr. Martin J. McKeown for his guidance to my research. His insights in clinic, engineering and mathematics areas have inspired me in any possible way. Colleagues from Medical Image Analysis Lab at Simon Fraser University have major contributions to my projects. Special thanks to Dr. Ali R. Khan, who coached me when I first joined the lab, and worked with me through many projects over the years. Colleagues from Brain Research Center at University of British Columbia have provided valuable data and validation to my algorithms. Without their contribution my research would be impossible to complete. Last but not least, I want to thank my loving parents for their unconditional support to my academic career. I would not have come this far without them!

# Contents

# List of Tables

# List of Figures

# Chapter 1

# Introduction

## 1.1 Motivation

### 1.1.1 Parkinson's disease

Parkinson's disease is the one of the most common neurodegenerative diseases in Canada, which affects approximately 1% of the population above the age of 65 [1]. The symptoms of PD are caused by direct and indirect effects of unexplained premature degeneration of dopamine-producing cells in the midbrain. The original descriptions emphasized changes in the motor system, such as tremor, bradykinesia (slowness of movement) and rigidity, however, it is becoming increasing apparent that other symptoms like dementia may also appear in the advanced stages of PD [2]. Despite numerous attempts, it is still unclear whether any treatments actually modify the inexorable progression of the disease as opposed to merely treating the symptoms, making quantitative measurements of disease severity in PD vital. However, diagnosis of PD is still based on clinical criteria, and attempts to obtain quantitative markers of disease progression to assess the effects of potentially disease-modifying therapy have been disappointing because 1) they cannot dissociate the beneficial effects of symptomatic treatment from disease progression, 2) they are expensive or use technology that is only available in specialized centers, and 3) despite being quantitative, they correlate poorly with overall disability, possibly because disease progression and compensatory

[1] Parkinson Society Canada `http://www.parkinson.ca/site/c.kgLNIWODKpF/b.5184077/k.CDD1/What_is_Parkinsons.htm`

[2] Wikipedia `http://en.wikipedia.org/wiki/Parkinson's_disease`

mechanisms are confounded. In this thesis, we present novel analysis methods applied to Magnetic Resonance Imaging (MRI) scans that attempts to address the above concerns.

### 1.1.2 Brain morphometry

Brain morphometry analysis is concerned with the quantification of anatomical features derived from brain imaging procedures, such as MRI. Parkinson's Disease is an ideal condition for quantitative morphometric analysis, as unlike Alzheimer's disease, the morphological changes in PD are typically not obvious, even to the trained eye. Thus quantifiable methods are required to determine if robust changes in brain structure exist in PD.

Brain morphometry studies are usually based on brain image segmentation, which is the process of assigning a label to a set of different anatomical structures on brain images. Commonly-used brain image segmentation methods can be categorized into three general types. The first type is knowledge-based, in which label assignment is based on implicit or explicit anatomical knowledge, such as training sets and anatomical constraints (Pitiot et al.[80]), shape and positional information (Xia et al.[103]) and landmarks (Chupin et al.[29]). The second type is template-based, whereby a pre-labeled template brain image is used to propagate labels to target brain images by a registration process between the template and the volume to be labeled. Previous attempts using this approach include Hierarchical Attribute Matching Mechanism for elastic registration (HAMMER) [88], and the Mindboggle method which utilized manually labeled brains as templates [63]. The third type is probabilistic-based, and estimates label assignment based on maximization of *a posteriori* probability of classification under certain constraints. Such methods have been proposed by Gouttard et al., who used a segmentatoion method via a deformable registration of an unbiased atlas with probabilistic spatial priors [48]. Fischl et al. presented a set of brain MR image reconstruction tools called FreeSurfer(FS) [40], which transforms target brain scans into Talairach space and performs both cortical percolation and subcortical segmentation. Khan et al. [62] developed the fully automated FS+LDDMM method that combines the probabilistic-based FS method with Large Deformation Diffeomorphic Metric Mapping (LDDMM) based label propagation [8]. The FS+LDDMM method computes the deformation between the ROIs of template and target images, then uses the same deformation to map the known anatomy information (manual labels) from the template brain onto target brains, thus generating the segmentation, as is shown in Figure 1.1.

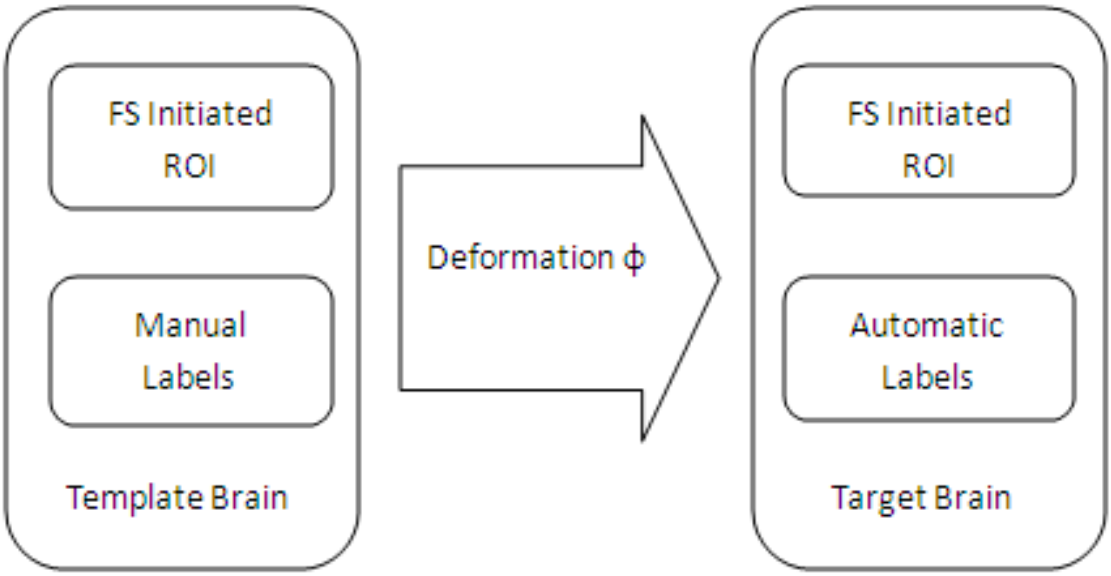


Figure 1.1: Mechanism of FS+LDDMM method. Note that the inverse deformation is used to find out the template-brain coordinates where each voxel of the segmentation result originates. Usually the coordinates point to non-grid locations in the template brain(s) and interpolation is required. Using the deformation directly cannot guarantee each voxel in the template brain can be mapped to a grid location in target brain.

We tested the segmentation accuracy of FS+LDDMM and FS-alone with six ROIs including the caudate, thalamus, and putamen (both left and right) from 26 clinical T1 scans (14 PD subjects and 12 age-matched control subjects without neurologic disease) that had also been manually segmented by a trained neuroscientist [24].

We used several comparison metrics to quantify the segmentation accuracy, as shown in Equation 1.1 - 1.6. The $L1$ error is defined in Equation 1.1, where we denote a manual segmentation by $M$ and an automatic segmentation by $A$. The Dice Similarity Coefficient (DSC) is defined in Equation 1.2, with $V(A)$ representing the volume of the segmented image $A$. It is assumed $A$ and $B$ are binary segmentations. With this formulation, perfect spatial correspondence between the two binary images would result in $DSC = 1$, and no spatial correspondence would result in $DSC = 0$. We also computed the Symmetrized Hausdorff Distance and the Symmetrized Mean Surface Distance. The Directed Hausdorff Distance

is defined in Equation 1.3 , where $d(a, b)$ is the distance between points on two different surfaces. To symmetrize this metric, we use Equation 1.4. The Hausdorff Distance gives an upper bound on the mismatch between the contours of segmentations. Directed mean surface distance is defined in 1.5, and is symmetrized similarly as Equation 1.6.

$$Error_{L1} = \frac{\|A - M\|_{L1}}{\|M\|_{L1}} = \frac{\sum_{x\in\Omega} \|A(x) - M(x)\|}{\sum_{x\in\Omega} \|M(x)\|} \tag{1.1}$$

$$DSC(A, B) = \frac{2V(A \cap B)}{V(A) + V(B)} \tag{1.2}$$

$$h(A, B) = \max_{a\in A} \min_{b\in B} d(a, b) \tag{1.3}$$

$$H(A, B) = \max\{h(A, B), h(B, A)\} \tag{1.4}$$

$$sd(A, B) = \frac{1}{N_A} \sum_{a\in A} \min_{b\in B} d(a, b) \tag{1.5}$$

$$SD(A, B) = max\{sd(A, B), sd(B, A)\} \tag{1.6}$$

A typical set of segmentation results are compared in Figure 1.2. Table 1.1 shows the overlap percentages (DSC and L1 error) for the FS+LDDMM, FS and manual segmentations. We assumed that the manual segmentation represents the "gold standard". For all ROIs, decreases in L1 error can be found in FS+LDDMM segmentations compared FS. For the majority of ROIs, improvement of the DSC can be found in the FS+LDDMM segmentations compared to the FS labels, which suggests that the FS+LDDMM segmentations have more similarity to manual segmentations than FS segmentations. Table 1.2 contains surface distances (the Hausdorff distance and mean surface distance) between both FS+LDDMM and FS segmentations to manual segmentations. For all ROIs, FS+LDDMM segmentations have smaller surface distances to manual segmentations over FS, which again is suggestive of improvement of segmentation accuracy.

### 1.1.3 Anatomical variability

One of the biggest challenges for brain morphometry methods in evaluating disease populations such as PD is to differentiate the PD-related group differences from the expected

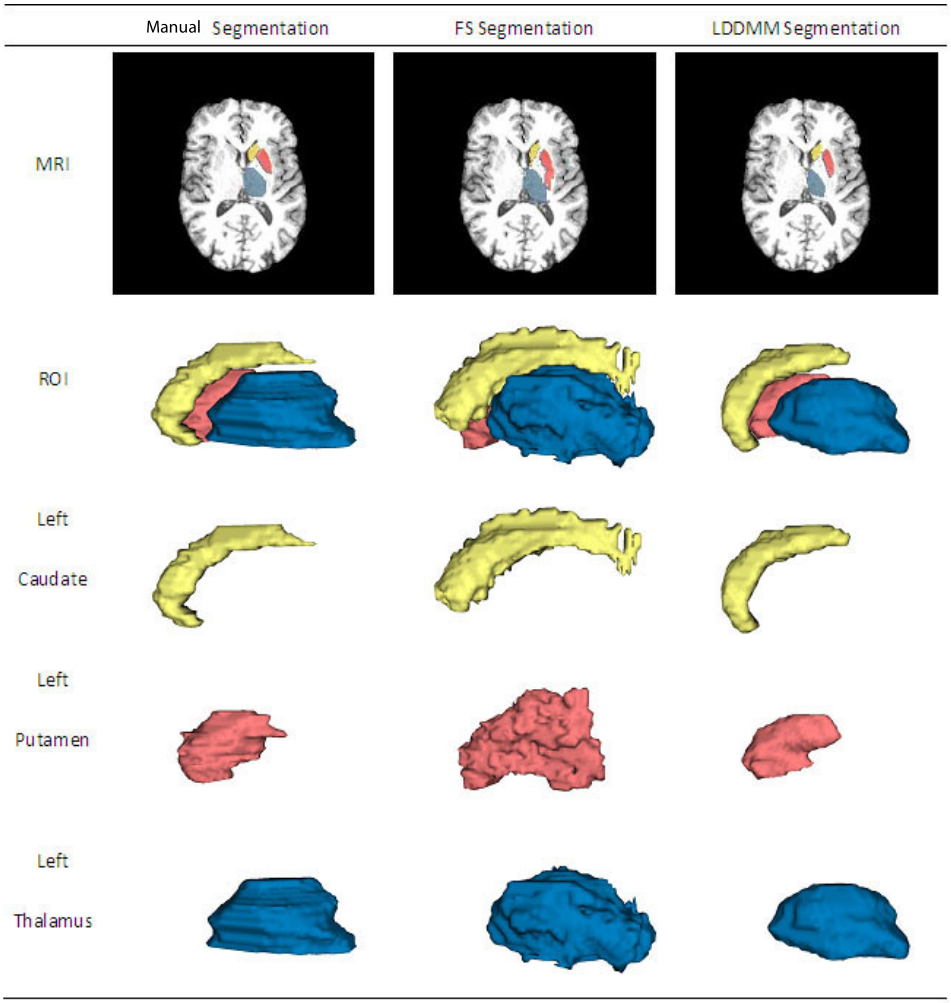


Figure 1.2: Surface visualization of segmentation results including manual segmentation *left column*, FS segmentation *middle column* and LDDMM segmentation *right column*. The first row is the original brain MRI slices overlapped with segmenting results (Transverse view). The second to fifth rows are the 3D volumes for the three Basal Ganglia structures (Sagittal view). The second row is three structures posed in respective positions. The third row to fifth rows contain the caudate, putamen and thalamus segmentations respectively.

Table 1.1: Average DSC's and L1 errors of FS-segmented structures and LDDMM-segmented structures using manually segmented structures as references

| Structure/Manual volume | Method | Volume | DSC | L1 error |
|---|---|---|---|---|
| Left Caudate/ | FS | $3818 \pm 556.12$ | $0.68 \pm 0.08$ | $0.38 \pm 0.16$ |
| $3177 \pm 999.36$ | FS+LDDMM | $2899 \pm 443.94$ | $0.75 \pm 0.07$ | $0.24 \pm 0.07$ |
| Left Putamen/ | FS | $5246 \pm 751.23$ | $0.65 \pm 0.11$ | $0.51 \pm 0.26$ |
| $3330 \pm 1254.47$ | FS+LDDMM | $2077 \pm 517.83$ | $0.67 \pm 0.11$ | $0.27 \pm 0.06$ |
| Left Thalamus/ | FS | $7186 \pm 838.22$ | $0.73 \pm 0.08$ | $0.37 \pm 0.21$ |
| $4840 \pm 1131.67$ | FS+LDDMM | $4410 \pm 514.89$ | $0.74 \pm 0.06$ | $0.26 \pm 0.10$ |
| Right Caudate/ | FS | $3586 \pm 523.71$ | $0.68 \pm 0.06$ | $0.34 \pm 0.12$ |
| $3282 \pm 978.63$ | FS+LDDMM | $3176 \pm 432.14$ | $0.71 \pm 0.06$ | $0.29 \pm 0.08$ |
| Right Putamen/ | FS | $4803 \pm 786.12$ | $0.69 \pm 0.09$ | $0.40 \pm 0.21$ |
| $3439 \pm 1278.78$ | FS+LDDMM | $3388 \pm 648.38$ | $0.71 \pm 0.06$ | $0.30 \pm 0.09$ |
| Right Thalamus/ | FS | $6942 \pm 668.06$ | $0.74 \pm 0.07$ | $0.33 \pm 0.18$ |
| $5175 \pm 1193.04$ | FS+LDDMM | $5005 \pm 523.20$ | $0.72 \pm 0.08$ | $0.29 \pm 0.12$ |

within-group, inter-subject anatomical variability. Conventional methods typically involve normalization i.e. spatially transforming different brain scans to a standard space for purposes of atlas alignment, inter-subject averaging, or characterization of anatomical structures. In fMRI analyses, time series from different subjects are concatenated together under the assumption that there is a perfect correspondence at the voxel level across subjects after normalization. Often data are spatially smoothed to make this assumption less rigid, but this degrades the spatial resolution. Standard low dimensional methods for spatial normalization can result in significant misregistration, particularly for smaller structures such as those of the basal ganglia, which constitute a significant proportion of the ROIs in PD studies.

To rigorously assess the residual anatomical variability in basal ganglia structures after standard spatial normalization, we studied the extent of RAV in 6 basal ganglia structures from 27 brain scans after spatial normalization by Freesurfer [40], Statistical Parametric Mapping (SPM)[6], and Large Deformation Diffeomorphic Metric Mapping [8]. In our study [23], we used the extended DSC to measure the overlap percentage of normalized ROIs under template space. The extended DSC is defined as:

$$DSC(S,n) = n \times V(\bigcap_i S_i) / \sum_{i=1}^{n} V(S_i) \tag{1.7}$$

where $S_i, (i = 1, 2 \dots n)$ are ROIs from subject $i$ in this paper. $V(S_i)$ is the number of

Table 1.2: Average Hausdorff distances and mean surface distances of FS-segmented structures and FS+LDDMM-segmented structures using manually segmented structures as reference

| Structure | Method | sym hausdorff | sym 95% hausdorff | sym mean surf dist |
|---|---|---|---|---|
| Left Caudate | FS | $16.85 \pm 5.86$ | $12.01 \pm 5.94$ | $2.92 \pm 1.59$ |
| | FS+LDDMM | $6.68 \pm 3.27$ | $4.41 \pm 2.64$ | $1.38 \pm 0.63$ |
| Left Putamen | FS | $11.93 \pm 3.49$ | $8.76 \pm 3.26$ | $2.90 \pm 1.29$ |
| | FS+LDDMM | $8.36 \pm 3.93$ | $5.85 \pm 3.17$ | $1.95 \pm 0.97$ |
| Left Thalamus | FS | $7.44 \pm 1.59$ | $5.27 \pm 1.51$ | $2.11 \pm 0.67$ |
| | FS+LDDMM | $5.86 \pm 1.54$ | $4.35 \pm 1.21$ | $1.65 \pm 0.40$ |
| Right Caudate | FS | $16.26 \pm 5.41$ | $10.63 \pm 4.98$ | $2.57 \pm 1.21$ |
| | FS+LDDMM | $6.98 \pm 3.71$ | $4.44 \pm 2.65$ | $1.52 \pm 0.66$ |
| Right Putamen | FS | $10.84 \pm 3.72$ | $8.16 \pm 3.52$ | $2.46 \pm 1.18$ |
| | FS+LDDMM | $7.56 \pm 2.64$ | $5.23 \pm 2.02$ | $1.76 \pm 0.55$ |
| Right Thalamus | FS | $7.33 \pm 2.17$ | $4.93 \pm 1.82$ | $1.98 \pm 0.67$ |
| | FS+LDDMM | $6.71 \pm 1.56$ | $4.72 \pm 1.46$ | $1.88 \pm 0.53$ |

non-zero voxels of of $S_i$ (i.e. the volume of ROI $S_i$), and $n$ is the number of subjects to overlay, which we will refer to as the group size. When $n = 2$, the extended DSC becomes the standard DSC defined in Equation 1.2. For complete overlap between two segmentations, $DSC = 1$, and for no overlap, $DSC = 0$. We computed the average DSC of normalized ROIs using Nieto-Castanon's scheme [77]. Average DSCs were computed over all possible subject combinations.

The average DSCs of ROIs after three different spatial normalization methods are shown in Figure 1.3. As expected, smaller ROIs such as the globus pallidus had increased RAV when computed over all subject pairs with different group sizes and registration methods. The LDDMM method had the lowest RAV of the three methods, but was the most computationally intensive. For low dimensional registration methods such as the affine registration implemented in Freesurfer and SPM, RAV becomes a problem particularly as the group sizes increases. This result also has major implications for group fMRI studies that utilize spatial normalization as a standard pre-processing method, and supports the use of fMRI ROI analysis methods that compute significance in each subject's native space, especially when basal ganglia structures are involved.

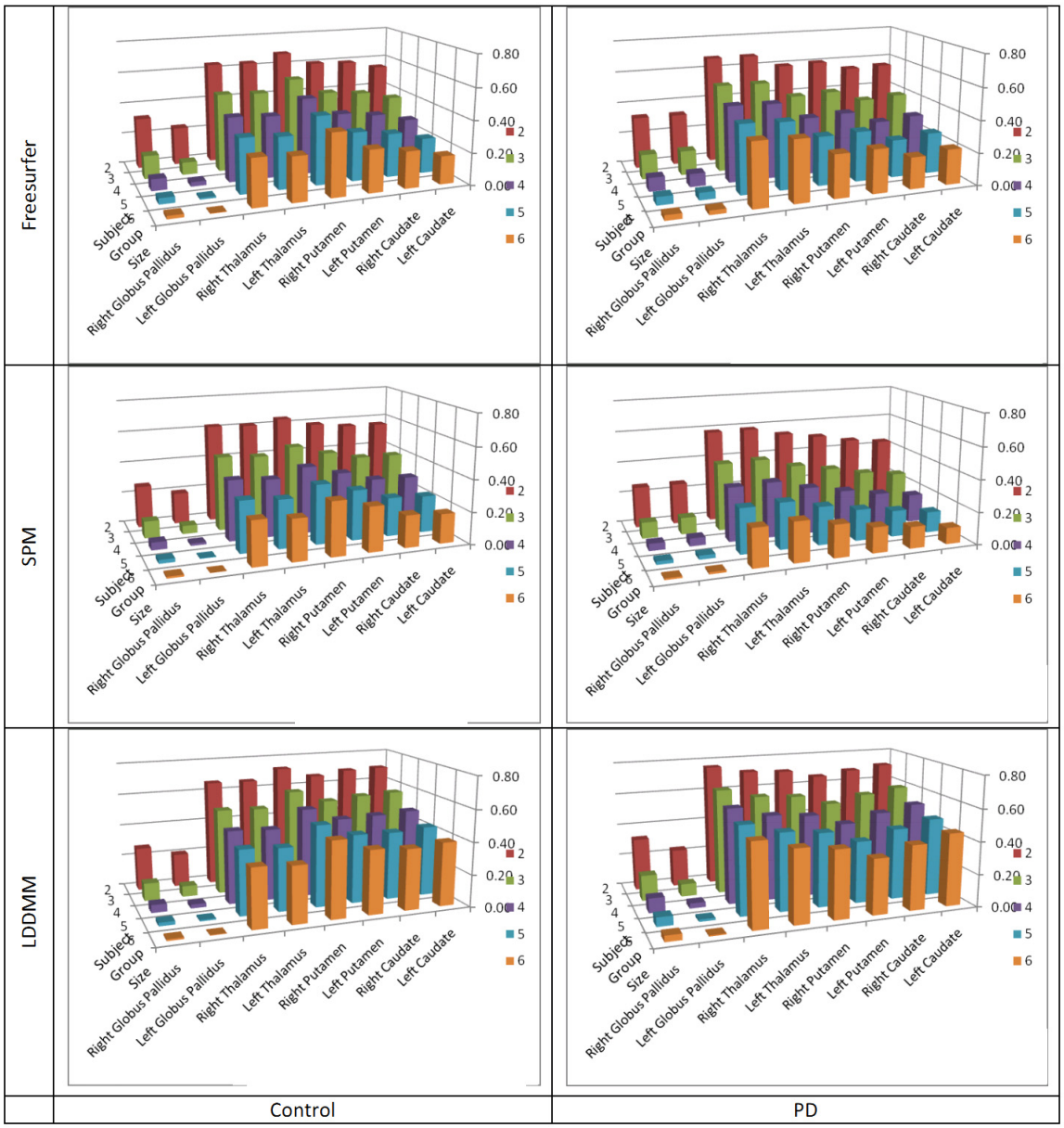


Figure 1.3: Average DSCs of registered ROIs. The rows correspond to different registration methods, from up to down is Freesurfer, SPM, LDDMM. The left column is control subjects and right column is PD subjects. For all ROIs, DSC decreases as group size grows. But the decrease is slower for high dimensional registration method LDDMM than low dimensional affine method used in Freesurfer and SPM.

In this thesis we present methods to 1) implement more accurate registration methods to reduce anatomical variability, 2) provide ways to both isolate anatomical variability from other information (e.g. Diffusion Tensor Data) and 3) analyze residual anatomical variability.

## 1.2 Thesis structure

The rest of thesis is organized as follows: Chapter 2 is focused on the analysis of on structural MRI analysis, including the FS-LDDMM automated brain segmentation algorithm and initial momentum analysis as a potential biomarker for Parkinson's disease. Chapter 3 describes a multi-structure registration algorithm, and applies it to susceptibility weighted imaging (SWI). Chapter 4 describes diffusion tensor image (DTI) analysis, including the implementation of Fukunaga-Koontz Transformation on co-registered DTI and MRI images. In Chapter 5 we summarize our research and give directions to future work. Finally in Appendix A we introduce fPipe, the automated toolbox for fMRI signal preprocessing, which includes the FS+LDDMM brain image segmentation method.

## 1.3 Thesis contributions

This thesis includes the following innovative contributions:

- Proposed and validated a method, based on analysis of the initial momentum of subcortical deformation to a template, as a potential biomarker in PD (Chapter 2).
- Developed a novel ICA approach for multi-structure initial momentum biomarker (Chapter 2).
- Developed a new method of multi-structure LDDMM registration and analysis of SWI data (Chapter 3).
- Developed a new method for separating DTI changes due to mis-registration and disease effects based on the Fukunaga-Koontz Transform (Chapter 4).
- Developed a fully-automated computational tool for fMRI data processing: fPipe (Appendix A).

# Chapter 2

# Structural MRI Image Analysis

## 2.1 Introduction

The commonly used brain morphometry methods to assess progression of disease, such as Parkinson's disease, can be categorized into three general types: voxel-based, surface-based, and deformation-based. By far, the majority of morphometry studies to date have been based on voxel-based morphometry (VBM), whereby subject brain images are registered to a common template image, and statistical analyses are performed on a voxel-by-voxel basis on the registered subject brain image. This technique has demonstrated cortical loss in some brain areas in PD [17][74] and in other diseases that may mimic PD [79][16][97]. Nevertheless there is greater recognition of the limitations of VBM, and a trend toward methods that attempt to analyze brain regions in their original shape (e.g. [38]), as we describe in this chapter. Imperfect registration to a template, as we demonstrated in Chapter 1 and in [24], results in questionable interpretations from VBM[14]. Also, VBM tends to be biased to find focal changes as opposed to more spatially distributed changes [35], and may be insensitive to subtle morphological alterations [12]. We show in this chapter that morphological changes tend to be distributed across many portions within an ROI, and across several ROIs simultaneously.

One way to mitigate the problems associated with VBM is to utilize surface-based morphometry (SBM). In SBM, a surface representation of structural boundaries is used instead of a one-to-one registration, which makes it more robust to subtle misregistration. Using such a method, Apostolova found PD related shape and volume changes correspondingly by SBM [5]. Similarly, McKeown et al. used a novel spherical harmonic based representation

of manually-segmented structures to demonstrate significant shape (although not volume) changes in PD [72].

Deformation-based morphometry (DBM) is an alternative way to avoid losing potentially important information during the registration process, but requires one-to-one, highly non-linear registrations to get sufficient accuracy. In DBM, instead of analyzing the registered subject brain images directly, the deformation fields, or the initial momentum field of the registration process are analyzed. Duchesne proposed a DBM method based on a volume of interest (VOI) that encompassed the hindbrain [37]. However, because multiple structures were partially or entirely included in the VOI, it's difficult to locate the shape changes of each individual structure, making biological interpretation difficult. In this chapter, we present a DBM method that uses anatomically-defined regions of interest (ROI) instead of a non-biologically defined VOI which may contain many types of structures.

## 2.2 Methods

The proposed method consists of the sequential application of a number of steps, which are briefly summarized below and subsequently expanded in the following sections. Regions of interest (ROIs), corresponding to known anatomical regions, are first segmented from anatomical images. While this could be done automatically, here we use manually segmented ROIs to avoid inducing unwanted sources of variability in the results. A "typical" control subject is chosen from amongst the subjects to act as a template. Large Deformation Diffeomorphic Metric Mapping (LDDMM) is then used to register the ROIs from this template to all other subjects' ROIs. The initial momentum of the deformation field is then used as a morphological feature. We concentrate on the voxels on the surface of the binary mask marking the ROIs, which tend to have the greatest variability in deformation, to reduce dimensionality. The *(x,y,z)* coordinates of the deformation field from the surface are then concatenated into a single row vector. Row vectors from different subjects are then collected into a matrix. Independent Component Analysis (ICA) is then applied to determine the independent deformation fields that are distributed in various amounts across subjects. The loading across subjects of the independent deformation fields are then assessed for their discriminative value and/or their correspondence with clinical attributes. These individual steps are expanded below.

### 2.2.1 Data acquisition and segmentation

We acquired 42 T1-weighted whole-brain MR images from a 3 Tesla scanner (Philips Achieva 3.0T; Philips Medical Systems, Netherlands), (3-D SPGR, TR = 14 ms, TE = 7.7 ms, flip angle = 25°), with voxel dimensions 1.0 x 1.0 x 1.0 mm, 176 x 256 voxels, 170 slices axially parallel to the AC-PC plane. The subject cohort consisted of two groups: 19 subjects with a clinical diagnosis of Parkinson's Disease (PD), and 23 age-matched control subjects with no known neurological or psychiatric conditions.

Four basal ganglia ROIs (putamen, caudate, thalamus, globus pallidus) in each hemisphere were outlined manually by a trained research assistant using anatomical atlases and Amira software (Amira 3D Visualization and Volume Modeling V.3.1.1.) as shown in Figure 2.1. The research assistant was blinded to the diagnosis. To test the consistency of the manual segmentation, we required the research assistant to segment one control subject 5 times independently. The overlap percentage of same ROI segmented in different session is very high (DSC$>$ 90%), indicating high consistency of manual segmentation.

### 2.2.2 Template selection

The segmented ROIs are registered with Large Deformation Diffeomorphic Metric Mapping (LDDMM) [8]. The LDDMM requires a template and other ROIs to be registered. We employed the following method to choose a "representative" subject. All ROIs from this representative subject ROIs were then used as templates. For each subject, we computed the following quantity:

$$C_i = \sum_{j=1}^{N} [\frac{(V_i(j) - \overline{V^j})}{\overline{V^j}}]^2; \tag{2.1}$$

where $N$ is the number of ROIs, $V_i^j$ is the volume of ROI $j$ in subject $i$, and $\overline{V^j}$ is the median volume size of ROI $j$ in the whole subject group. $C_j$ therefore represents the normalized distance of subject $i$ to the group median volume, averaged over all ROIs. The subject with the minimum $C$ value was then chosen as the representative subject. Figure 2.2 shows the subject with smallest $C$ (0.15). It can be seen from the figure the volumes of all 8 ROIs of this subject are very close to median volumes in the histogram. While the goal of this template selection method is to provide maximum discriminating power of deformation field and initial momentum, a more sophisticated method is to compute a group average

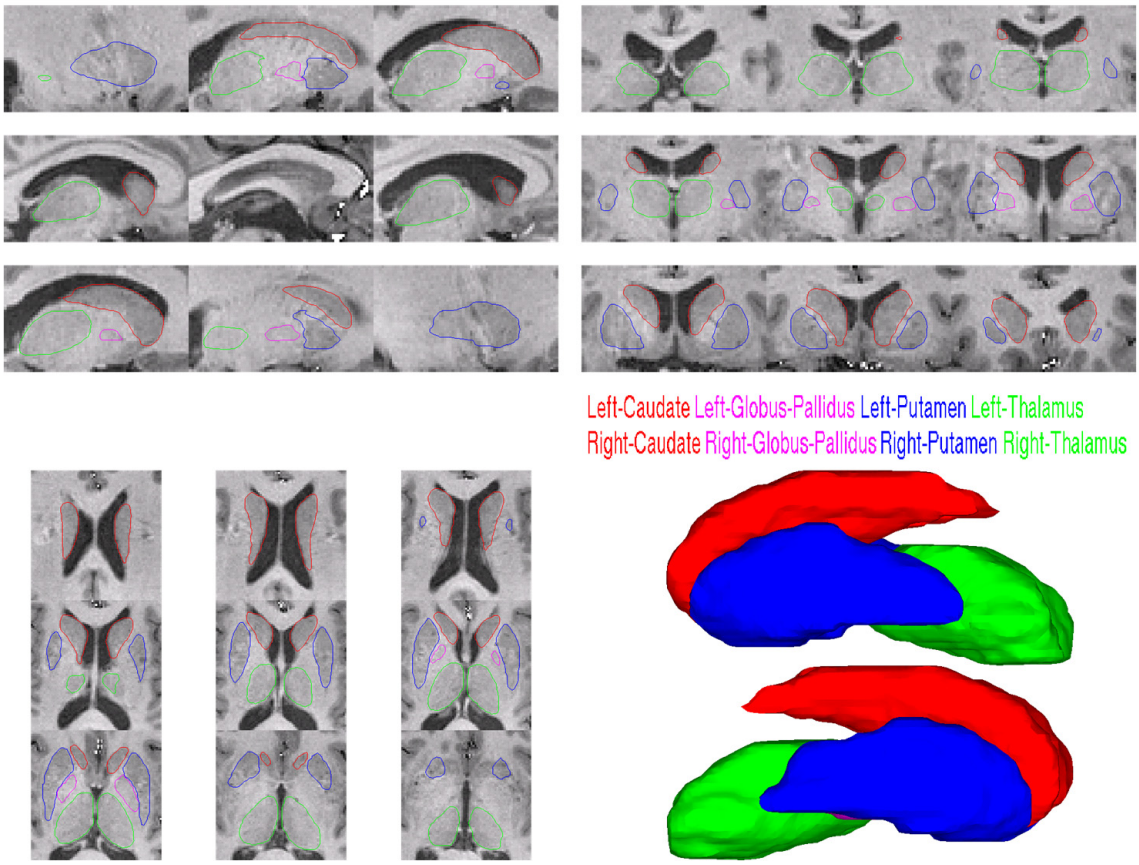


Figure 2.1: Visualization of the ROI network of a typical normal control subject. A 3x3 slice array is displayed for each of the Sagittal (upper left), Coronal (upper right) and Axial (lower left) view. The colored 3D surfaces of ROIs are shown at lower right, caudate is red, putamen is blue, thalamus is green and pallidus (most part covered by putamen) is magenta.

template [61] as introduced in Chapter 4.

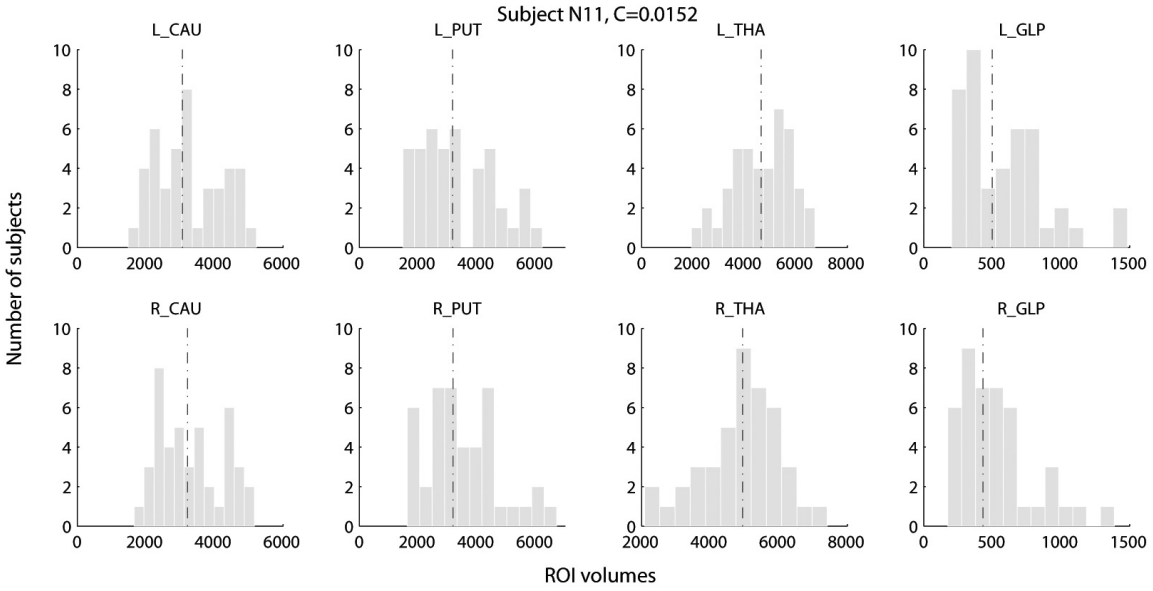


Figure 2.2: Volume histogram of 8 ROIs. The dash dot line indicates where the ROI volumes of the representative subject is located on the histograms of whole group.

### 2.2.3 Feature extraction

In the framework of computational anatomy (CA) [49], images can be defined as a function $I : \Omega \to \mathbb{R}$, where $\Omega \in \mathbb{R}^3$ is the domain of the voxel in 3D volume. Let the operator $\Psi$ represent the process of segmentation of an image that yields a labeling $\Psi : \Omega \to \mathbb{Z}$, mapping each voxel of the image with an integer label for the subcortical structure to which the voxel belongs. LDDMM [8] finds the geometric transformation $\varphi_j : \Omega \to \Omega$ such that each target image $I_j, j = 1 \cdots N$ is registered accurately to the template $I_0$; i.e. $I_0 \circ \varphi_j^{-1} \approx I_j$ minimizing an appropriate metric such as $\|I_0 \circ \varphi_j^{-1} - I_j\|_{L^2}$, where $\|\dot{\|}_{L^2}$ is the $L^2$ norm in the space of functions $I$.

Given the segmentation of a particular structure in the template $I_0$, the corresponding structure in target space can be computed by transforming the manual template segmentation, $\Psi^{man}(I_0) \circ \varphi_j^{-1}$.

Miller proved [73] that the LDDMM geodesic follows the property of conservation of

momentum, which takes the form of

$$(L^\dagger L)v_t = |D\phi_{t,0}|(D\phi_{t,0})^t(L^\dagger L)v_0 \circ \phi_{t,0} \tag{2.2}$$

where $(L^\dagger L)v_t$ denotes the momentum of the evolving template transformation at time $t$. The knowledge of the initial momentum $(L^\dagger L)v_0$ with which the template coordinates evolve completely specifies the full geodesic connecting the given template and target images. Hence, the initial momentum encodes the shape and form of the target. In particular, this allows linear techniques such as ICA to be applied to statistical analysis of the initial momentum that encodes the target shape. Instead of performing ICA analysis under the $L_2$ metric, we performed it with respect to the metric in space used for the estimation of the flow [101], i.e. the quantity $Lv_0$.

In this paper we performed LDDMM using flows discretized to 20 time-steps, parallelized on 8-processors for each ROI to compute the diffeomophism and initial momentum of each individual structure.

### 2.2.4 Dimension reduction

Empirically, we observed that volumetric vector field of initial momentum was sparse, with only the vectors near the boundary of the ROIs having significant non-zero entries. We therefore utilized an isosurface mask to reduce the dimension of the initial momentum feature vectors. We create a mask based on the template ROI isosurface, defined as $Mask(V) = Dilation(V) - Erosion(V)$, where $V$ is a binary image of ROI.

### 2.2.5 Independent component analysis

ICA is a decomposition method to model mixed signals as the linear superposition of independent components. Let $X$ be the masked initial momentum matrix with the rows representing the deformation for each subject. ICA decomposes the matrix $X$ into a mixing matrix $A$ and independent components $s$ so that $X = As$, and the rows of matrix $s$ are maximally linearly independent. Because of the stochastic nature of the learning process, the computed ICs can vary slightly from different session to session, particularly if they represent a small amount of the original variance. One approach to deal with this problem is to perform repeated analysis on the same data set, and check for the consistency of the

extracted components. We used the ICASSO package for Matlab to [51] compute stable ICs.

The columns of $A$ represent the loadings i.e., the contribution of each independent deformation pattern (represented as rows of $s$) to each subject's overall deformation pattern. To assess the clinical significance of the independent deformation patterns, we can assess whether or not the loadings correlate with clinical indices, such as measures of disease progression, age, amount of drug necessary to treat symptoms, etc.

The correlation coefficient of loadings on the ICs and clinical indices can thus be computed as:

$$r(a,c) = \frac{Cov(a,c)}{\sqrt{Cov(a,a)Cov(c,c)}} \tag{2.3}$$

where $a$ is a single column of the unmixing matrix $A$, and $c$ is a clinical indices vector, and $Cov()$ is the covariance function.

The t-statistic and level of significance (p-value) are computed as:

$$t = r * \sqrt{\frac{n-2}{1-r^2}} \tag{2.4}$$

$$p = 2(1 - tcdf(|t| \mid n-2)) \tag{2.5}$$

where $R$ is the correlation coefficient from equation 2.3, $n$ is the number of subjects, and *tcdf* is the Student's t cumulative distribution function.

To correct the threshold of significant level we use a rough False Discovery Rate (RFDR) [10]:

$$p^* = \frac{\alpha(m+1)}{2m} \tag{2.6}$$

where $\alpha = 0.05$ is the level of significance for single test, and $m$ is the number of independent tests.

To assess the clinical significance of the computed ICs of the deformation field, we examined the subject-by-subject loading on the different ICs and compared it to each subject's subscores in the Unified Parkinson's Disease Rating Scale (UPDRS). UPDRS is a scale of disease severity based on clinical examination [1], which includes scores on a number of

[1]National Parkinson's Foundation `http://www.parkinson.org/Professionals/Professional-Resources/Screening-Instruments`

domains including mentation, behavior, and mood, activities of daily living, and clinician-scored motor evaluation. In our study, we focused on the clinician-scored motor evaluation of rigidity and tremor over five body parts – head, left and right arm, left and right leg. Since the UPDRS of control subjects is 0 in all fields, to avoid bias, we only computed correlation coefficients for PD subjects' IC loadings and their UPDRS.

### 2.2.6 ROI network VS. separated ROIs

In order to jointly examine the feature vectors of all ROIs (caudate, putamen, thalamus and pallidus), we first concatenated the feature vectors from the individual ROIs to form a ROI network feature vector, and then performed ICA on combined feature vectors.

While this has the benefit of looking for changes across ROIs – of particular biological interest – it assumes that relative changes seen between ROIs will be consistent for all subjects. An alternative approach, which relaxes this assumption, but still allows statements to be made about consistent morphological changes across ROIs, is to perform ICA on each ROI feature vector separately, and then determine if there are similar subject loadings across the ROIs. Again, we used the ICASSO approach to determine the number of ICs reliably extracted for each ROI. Using a standard cutoff for the quality of the extracted components ($iq > 0.85$), we ascertained that each ROI had 2 stable ICs. The subject loadings on these ICs were collected, to create a $42 \times 16$ (2 ICs $\times$ 8 ROIs) matrix, $A_{all}$. Thus for each ROI, an ICA decomposition was performed: $X = As$; where rows of $s$ are the independent vector fields and columns of $A$ are the weighting on each subject. then: $A_{all} = [A_1^1, A_1^2, ..., A_8^1, A_8^2]$, where $A_i^j$ is the $j-th$ column of mixing matrix $A$ for ROI $i$. In order to find the ROIs that had similar loadings across subjects, we utilized the replicator dynamics equation [76]:

$$x_i(t+1) = x_i(t)\frac{(Cx(t))_i}{x(t)^T Cx(t)} \tag{2.7}$$

where C is the covariance matrix of $A_{all}$ with diagonal entries set to zero.

We start with a uniform distribution of membership, and the stable membership after 300 iterations is shown in Table 2.2. From the table we can see the ICs of left putamen (L_PUT), left thalamus (L_THA), right caudate (R_CAU) and right putamen (R_PUT) became dominant, i.e. the membership portion is larger than initial value (1/16) and stayed stable. Therefore the ICs of these four ROIs are co-varying. To assess the stability of these results, we performed a leave-one-out procedure (Figure 2.7) and re-ran the analysis until

it converged.

## 2.3 Results

### 2.3.1 Group differences on feature vectors

We initially assessed the feature vectors themselves to determine if they had discriminatory power. A voxelwise two-sample t-test was performed on the dot products of initial momentum and isonormals of ROI surface (i.e. the signed projection of initial momentum on isonormals) at same voxel. RFDR defined in equation 2.6 was used for the p value threshold to correct multiple comparisons. In this case $m$ equals to number of voxels masked by ROI isosurface, which ranged between 348 and 2098, depending upon the ROI. As result $p^* \approx 0.025$. Voxels of significant between-group differences ($p < p^*$) were detected in all ROIs. The mean t-statistic for significantly different voxels and the fraction of voxels within each ROI that demonstrated significant between-group differences is shown in Table 2.1.

| ROI | L_CAU | L_PUT | L_THA | L_GLP | R_CAU | R_PUT | R_THA | R_GLP |
|---|---|---|---|---|---|---|---|---|
| T-statistic | 2.47 | 2.42 | 2.38 | 2.49 | 2.43 | 2.41 | 2.36 | 2.35 |
| Fraction | 3.21% | 1.38% | 2.23% | 1.85% | 2.96% | 2.64% | 1.79% | 2.30% |

Table 2.1: The magnitude and fraction of significant between-group differences (in percentage).

From the table we can see the between-group difference in the left hemispheric ROIs are roughly equivalent to the homologous regions in right hemisphere in terms of magnitude and fraction of voxels that demonstrated significant group differences. To visualize the deformation pattern of ROIs that characterized the PD group, we color-coded the ROI isosurfaces where significant between-group differences ($p < p^*$) were detected. To emphasize small p values, we color-mapped the value of $-log(p)$. The display value is $sign(A)(-log(p))$ where A is 1 for voxels exhibiting hypertrophy in PD subjects vs controls (i.e. the dot product of the isonormal and the mean deformation for PD subjects was positive compared to controls) and -1 for the voxels indicating local atrophy (Figure 2.3). The t-statistics of voxel-wise group differences is also shown in Figure 2.4.

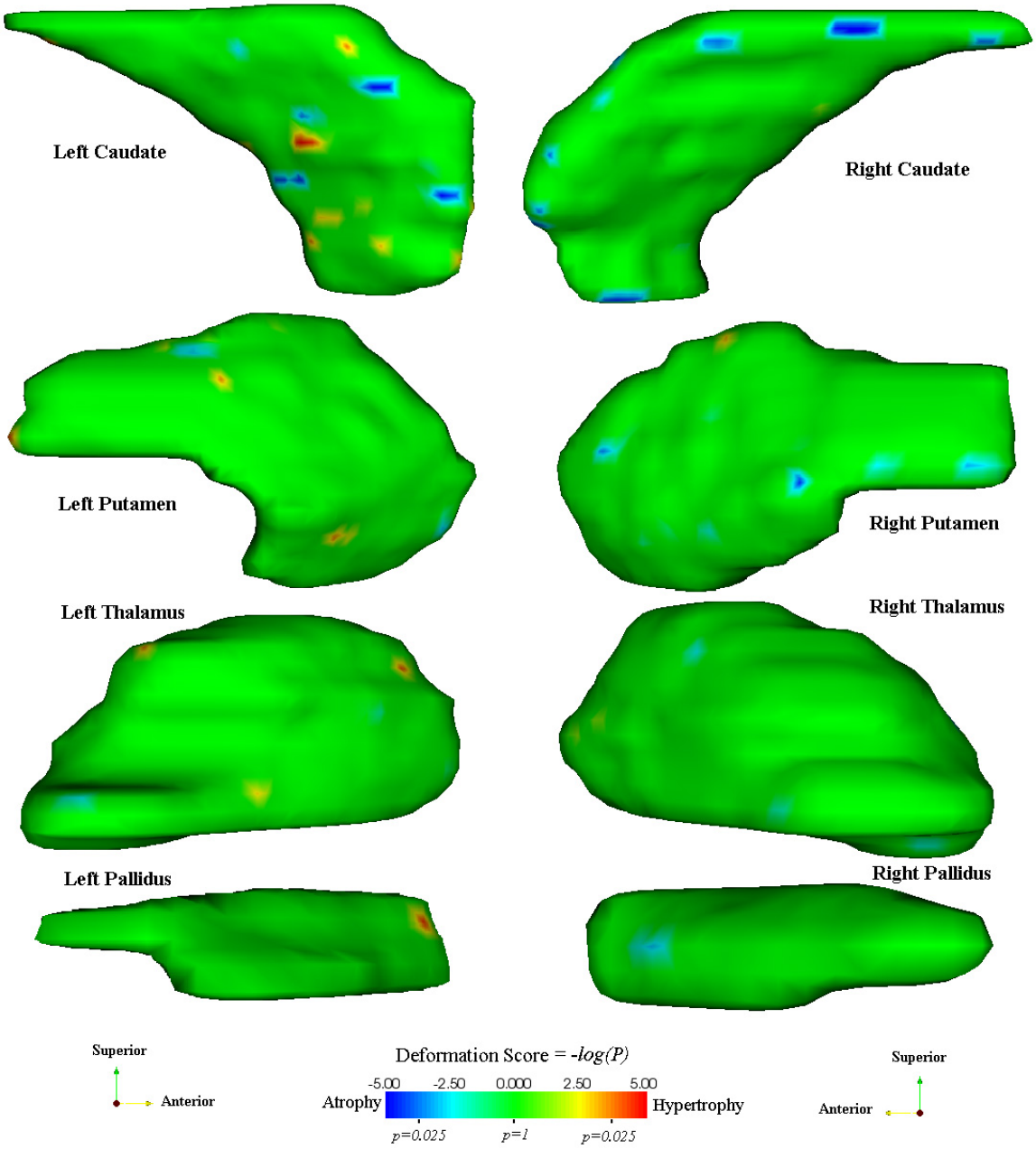


Figure 2.3: Colormap of deformation score representing significant between-group differences on ROI surfaces. The left column contains the left hemisphere ROIs, the right column contains the right hemisphere ROIs. Rows from top to bottom correspond to: caudate, putamen, thalamus and pallidus.

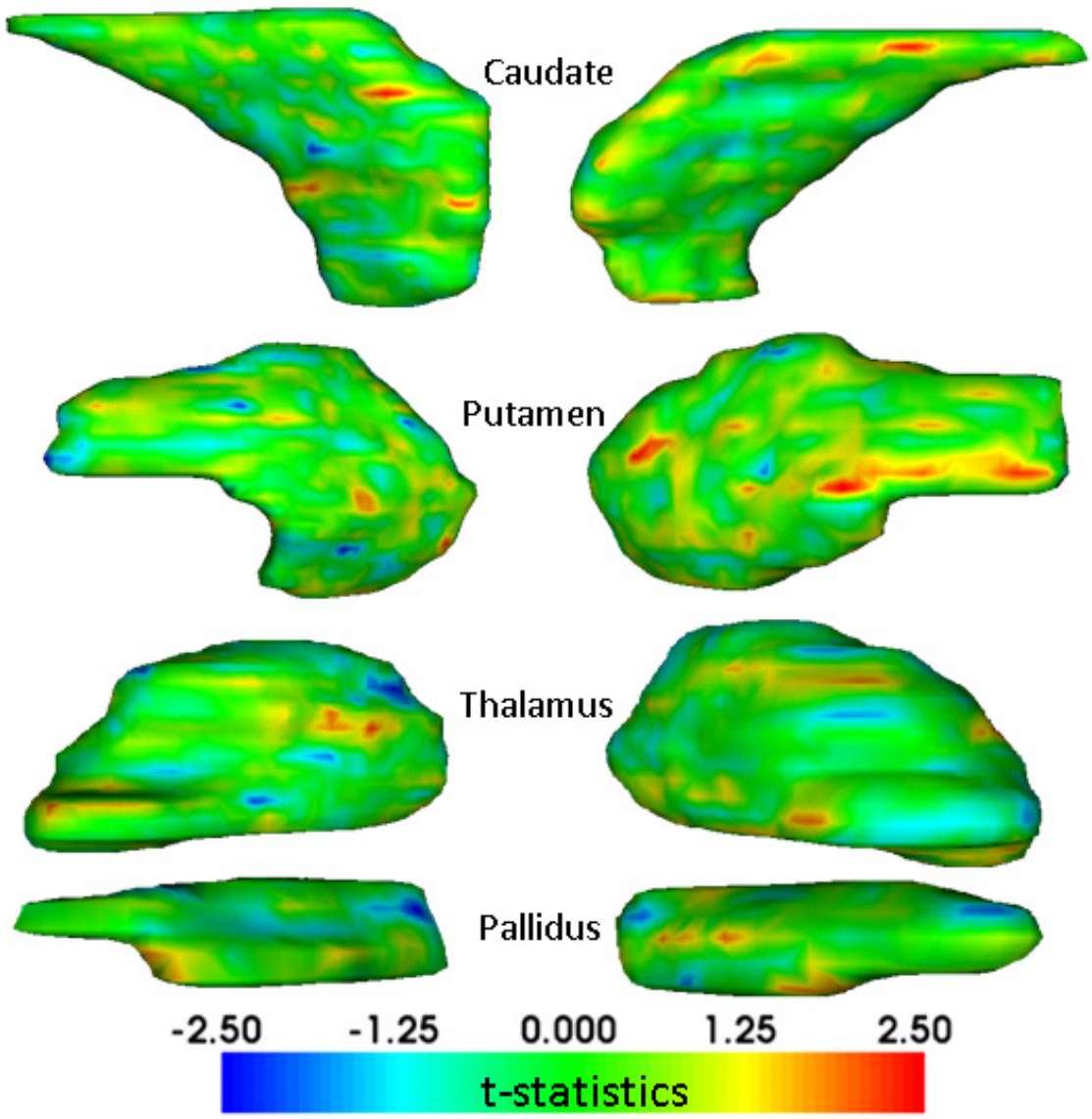


Figure 2.4: Colormap of T-statistics representing significant between-group differences on ROI surfaces. The left column contains the left hemisphere ROIs, the right column contains the right hemisphere ROIs. Rows from top to bottom correspond to: caudate, putamen, thalamus and pallidus.

### 2.3.2 Independent component analysis

We used the ICASSO package to decompose the initial momentum feature vectors into ICs [51]. ICs from a typical ROI (the left caudate) deformation are shown in Figure 2.5. By design, the ICs tend to have highly kurtotic distributions (i.e., probability distributions with narrow central peaks and large tails). For visualization purposes, we therefore restricted ourselves to voxels where the IC was more than three standard deviations from the mean. Note that in some ICs, many of those vectors with significant magnitude are located where significant between-group differences of ROI occurred using simple t-tests. In IC14, 15, 26 and 33, the clustered vectors on the left tip of this ROI overlap with a significant between-group difference area, which is on the back of ROI volume and therefore not shown on Figure 2.5.

The IC-UPDRS pairs with significant correlation are shown in Figure 2.6. For example, IC14 of all ROI concatenated initial momentum had a significant correlation (p=0.0211) to the head-rigidity term of subjects' UPDRS. Once we found the ICs correlated to the clinical indices, we mapped the ICs back to the original initial momentum coordinates, and then overlaid the vector field on the ROI surfaces, as shown in Figure 2.5.

When the replicator dynamics were performed to look for common subject loadings seen across more than one ROIs, the same ICs (corresponding to ICs derived from ROIs: L_PUT, L_THA, R_CAU and R_PUT) were found to covary across all subjects. By cross checking Figure 2.6 and Table 2.2 we can see that one of the co-varying ICs, IC1 of left thalamus, when examined individually, has significant correlation with UPDRS: tremor right leg in the PD subjects.

| IC No. | L_CAU | L_PUT | L_THA | L_GLP | R_CAU | R_PUT | R_THA | R_GLP |
|---|---|---|---|---|---|---|---|---|
| 1 | 0 | 0.3585 | 0.1129 | 0 | 0.2222 | 0 | 0 | 0 |
| 2 | 0 | 0 | 0 | 0 | 0 | 0.3064 | 0 | 0 |

Table 2.2: Stable membership distribution of replicator dynamics

As a *post hoc* analysis, in order to determine the ability of ICA to extract clinically-meaningful deformation patterns, we compared ICA to other methods of decomposition of the feature factors. We repeated the analysis using Principal Component Analysis (PCA)

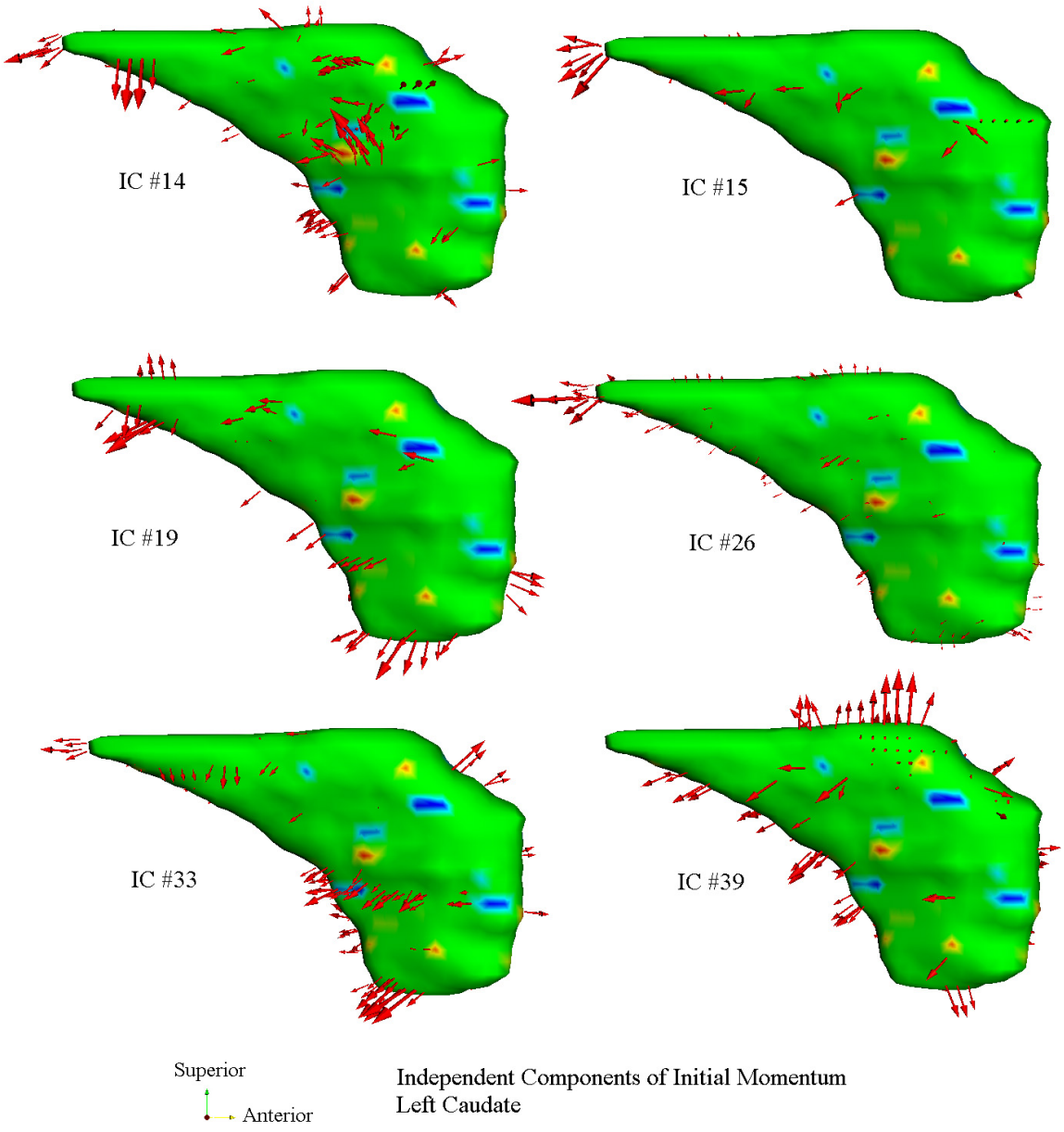


Figure 2.5: Independent components of initial momentum vector field, overlay on isosurface of left caudate. The size of arrows represents the vectors' magnitude.

| Clinical Indices / ICs | | Symptom Duration | UPDRS Rigidity Head | UPDRS Rigidity Left Arm | UPDRS Rigidity Right Arm | UPDRS Rigidity Left Leg | UPDRS Rigidity Right Leg | UPDRS Tremor Head | UPDRS Tremor Left Arm | UPDRS Tremor Right Arm | UPDRS Tremor Left Leg | UPDRS Tremor Right Leg | UPDRS Total |
|---|---|---|---|---|---|---|---|---|---|---|---|---|---|
| Left Caudate | 1 | | | 0.0220 | | | | | | | | | |
| | 2 | | | | | | | | | | 0.0108 | 0.0041 | |
| Left Putamen | 1 | | | | | | | | | | | | |
| | 2 | | | | | | | | | | | | |
| Left Thalamus | 1 | | | | | | | | | | | 0.0039 | |
| | 2 | | | 0.0192 | | | | | | | | 0.0133 | |
| Left Pallidus | 1 | 0.0146 | | | | | | 0.0029 | | | | | |
| | 2 | | | | | | | | | | | | |
| Right Caudate | 1 | | | | | | | | | | | | |
| | 2 | | | | | | | | | | | | |
| Right Putamen | 1 | | | | | | | | | | | | |
| | 2 | | | | | | | | | | | | |
| Right Thalamus | 1 | | 0.0012 | | | | | | | | | | |
| | 2 | | 0.0029 | | | | | 0.0178 | | | | | 0.0130 |
| Right Pallidus | 1 | | | | | | | | | | | | |
| | 2 | | | | | | | | | | | | |
| All ROIs Concatenated | 1 | | | | | | | | | | | | |
| | 2 | | | | | | | | | | | | |
| | 3 | | | | | | | | | | | | |
| | 4 | 0.0152 | | | | | | | | | | | |
| | 5 | | | | | | | | | | 0.0123 | | |
| | 6 | | | | | | | | | | | | |
| | 7 | 0.0072 | | | | | | 0.0017 | | | | | |
| | 8 | | | | | | | | | | | 0.0075 | |
| | 9 | 0.0146 | | | | | | | | | | | |
| | 10 | | | | | | | | | | | | |
| | 11 | 0.0194 | | | | | | | | | | | |
| | 12 | | | | | | | | | | | 0.0213 | |
| | 13 | | | | | | | | | | | | |
| | 14 | | 0.0211 | | | | | | | | | | |
| | 15 | | | | | | | | | | | | |
| | 16 | | | | | | | | | | | | |
| | 17 | | | | | | | | | | | | |
| | 18 | | 0.0129 | | | | | | | | | | |
| | 19 | | | | | | | | | | | | |
| | 20 | 0.0147 | | | | | | | | | | | |
| | 21 | | 0.0024 | | 0.0136 | | | | | | | 0.0107 | |
| | 22 | | | | | | | | | | | | |
| | 23 | | | | | | | | | | | | |
| | 24 | | | | | | | | | | | | |
| | 25 | | | | | | | | | | | | |
| | 26 | | | | | | | | | | | | |
| | 27 | | | | | | | | | | | | |
| | 28 | | | | | | | | | | | | |
| | 29 | | | | | | | | | | | 0.0045 | |
| | 30 | | | 0.0049 | | | | | | | | | |
| | 31 | | | | | | | | | | | | |
| | 32 | | | | | | | | | | | | |
| | 33 | | | | | | | | | | | | |
| | 34 | | | | | | | | | | | | |
| | 35 | | | | | | | | | | | | |
| | 36 | | | 0.0107 | | | | | | | | | |
| | 37 | | | | | | | | | | | | |
| | 38 | | | | | | | | | | | | |
| | 39 | | | | | | | | | | 0.0156 | | |
| | 40 | | | | | | | | | | | | |
| | 41 | | | | | | | | | | | | |

Figure 2.6: P-values of IC-loadings with correlation to clinical indices. Note only the p values of significant correlations are listed, the p values of insignificant correlations are left blank.

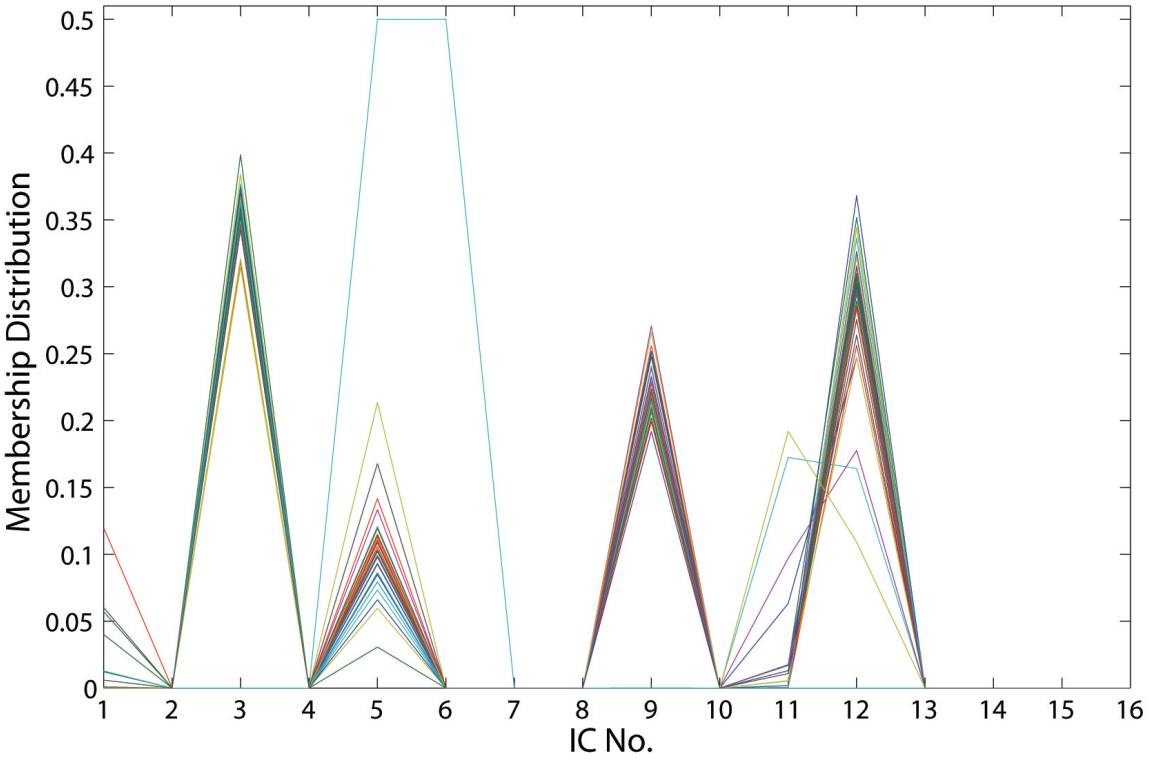


Figure 2.7: Leave-one-out replicator dynamics tests. Each colorful trail represents one test with one subject left out. The overlapping trails indicate the stability of converged membership.

as opposed to ICA and determined the correlation between the PC loadings and clinical indices. Since correlations are bounded, we performed Fisher's Z transform to the correlation between IC/PC loadings and UPDRS subscores to make their distribution approximately Gaussian, and then performed t-test to see if there were significant differences. The PC were found less well correlated to UPDRS than the IC loadings ($p < 0.05$) indicating higher correlation coefficients between IC loadings and UPDRS sub-scores, compared to the correlations between PC loadings and UPDRS subscores.

Because the clinical indices may not be independent of one another, we also determined the best linear combination of clinical indices that correlated with each component loading, and did this for both PCA an ICA loadings. After using a Fisher-Z transform, we then tested the null hypothesis that the correlation coefficients from PCA loadings vs clinical indices and ICA loadings vs clinical indices were equal. The correlations coefficients from the ICA loadings were significant greater (p=0.039).

## 2.4 Discussion

A biomarker can be defined as characteristic that is objectively measured and evaluated as an indicator of normal biological processes, pathogenic process or pharmacological response to a therapeutic intervention. PD is in desperate need for accurate biomarkers [7]: PD subjects typically become symptomatic when more than 50% of dopaminergic neurons are lost, suggesting a prolonged presymptomatic period [105]. Early in the disease course, it can be difficult to differentiate PD from other conditions such as Essential Tremor (ET), multisystem atrophy (MSA), and progressive supranuclear palsy (PSP). Even if the correct diagnosis has been made, PD subtypes are associated with wide variability in disease course and rate of progression, so an objective marker would be helpful.

A number of biomarkers have been proposed for PD, including motor performance tests such as finger tapping, oculomotor measures, olfaction, electrophysiological measures, neuroimaging (MRI, PET, SPECT), transcranial sonography, cardiac MIBG scintigraphy, metabolomic measures, biochemical tests, and microarrays (for an extensive review see, [4]). However, clinical scales such as UPDRS may suffer from floor and ceiling effects and other non-linear relationships between disease severity and scores, and are unhelpful in the presymptomatic stage. The effects of L-dopa medication may confound interpretation of motor scores, and oculomotor measures such as saccades [54]. Olfaction is impaired in PD,

and may help differentiate between PD and other parkinsonian syndromes but is independent of disease severity and duration [91]. Postural responses to neck stimulation do not significantly differ between moderately affected PD subjects and controls [100]. Transcranial sonography may be a sensitive tool, but hyperechogenicity does not vary during the course of PD [11], is operator dependent, and is seen in 16% of subjects with ET (compared to 75% of PD subjects) [92].

There are many advantages to structural MRI as a potential marker for a range of deficits seen in PD. Structural MRI may assess brain systems associated with motor and non-motor deficits, providing a unified framework to assess the multiple and often disparate factors that may contribute to overall disability. Although several dozen case-control studies have focused on the structural MRI changes in PD, the results have been inconsistent. For example, there has been inconsistency in reported putamen atrophy (e.g.,[70][64][46] vs [47], [87]), caudate volume (e.g [70] vs [2][46][47][87]), and ventricular size (e.g. [90] vs [55]). As validation, we also measured the volume of the 8 ROIs in our study. The histograms of ROI volumes in Control and PD subjects are shown in Figure 2.8. The histograms of Control and PD largely overlap with each other, indicating low group difference of volume. We also performed group difference tests on ROI volumes between PD and control group. No significant difference ($p < 0.05$) was detected, as expected.

A key factor for the conflicting results of morphological changes in PD is that the relatively insensitive measure of overall volume has been used to assess changes in specific brain structures. As previously shown, the thalami in PD undergo statistically highly significant shape changes, even when there may be no significant differences in volume [72]. The reason that shape may change but not the volume is likely due to the fact that particular nuclei (e.g centre median-parafascicular complex in Parkinson's disease [50]) are involved, and thus, at the typical resolution of MRI, this does not result in significant changes in overall volume. Alternately, thalamic volume may actually increase as a compensatory mechanism when cortical regions are damaged [81] which may minimize overall volume changes, but still result in distinct shape changes.

Another important benefit of exploring shape changes as opposed to scalar volume changes is that it provides a multidimensional measurement, making it easier to disentangle the multiple factors that may influence morphology. Here we modeled each subjects ROI as a linear combination of basis deformations that were computed with the ICA algorithm. Since the loadings on some ICs correlated with clinical indices, but other ICs did

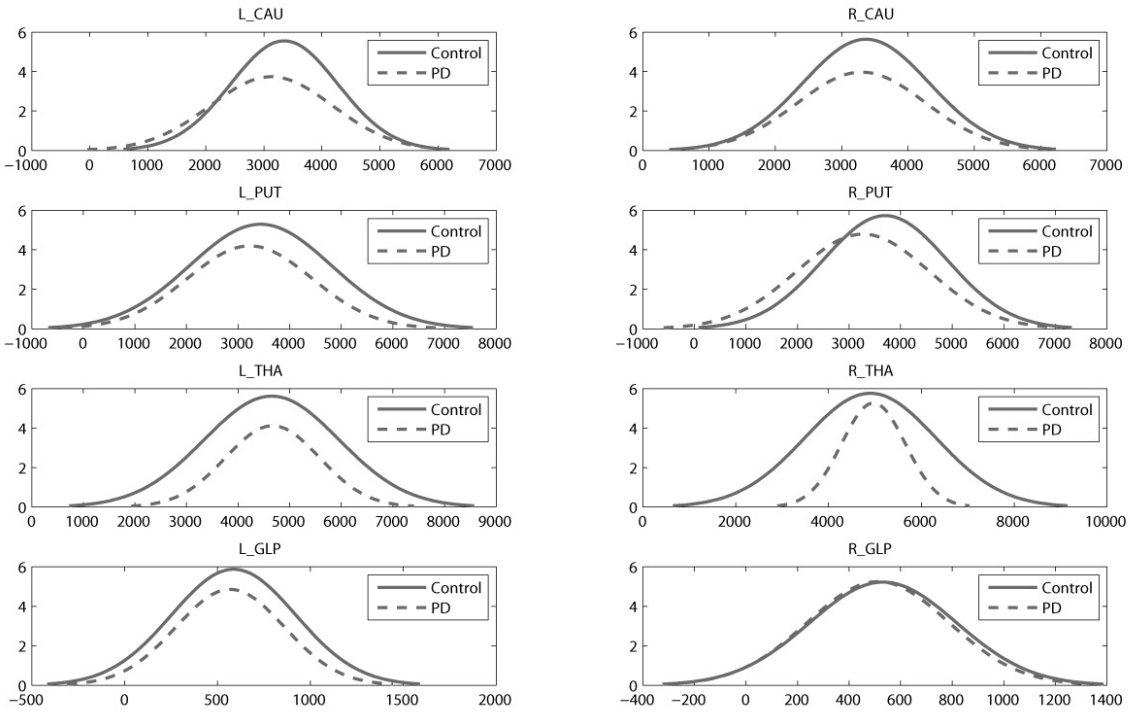


Figure 2.8: The normal fits of ROI volume histograms in Control and PD subjects. The histograms of Control and PD subjects largely overlap with each other, indicating low group difference of volume. The left column contains the left hemisphere ROIs, the right column contains the right hemisphere ROIs. Rows from top to bottom correspond to: caudate, putamen, thalamus and pallidus.

not, the proposed approach has the potential to decouple different sorts of shape variability (normal inter-subject variability, effects of normal aging, etc) from the effects of disease process itself. Currently most structural studies of disease states are longitudinal as looking at structural *changes* are one way to deal with the inherent inter-subject variability in ROI shapes. The current approach may allow the use of cross-sectional studies to assess disease-related morphological changes.

The current method is most similar to the method proposed by Wang et al.[101], whereby they applied principal component analysis (PCA) on the initial momentum features for Alzheimer's Disease and normal control subjects, and detected significant between-group difference on left hippocampus (p=0.0074), but no significant difference for right hippocampus (p=0.07). While we do not know the "ground truth" to directly compare the PCA and ICA techniques on the initial momentum fields, there are a number of reasons to suspect that ICA may be superior. We found a higher correlation between IC loadings and clinical indices compared to PC loadings and clinical indices suggesting that the ICs may have more biological significance. PCA assumes that the data are jointly Gaussian. In contrast, ICA will tend to find components that are highly non-Gaussian. Since we expect there to be focal changes in morphology, rather than broad overall changes (that could potentially be captured by volume calculations) we suggest that ICA is more appropriate for these types of data.

Similar to the current study, the recent morphometry analysis by Apostolova et al. also detected changes in basal ganglia structures between PD subjects with and without dementia[5]. Apostolova's method focused on volume, where the radial distance - an intuitive measure of the ROI thickness - was used as morphometric feature. In contrast, our proposed method focused on shape, where initial momentum - a measure of surface deformation pattern - was used as a morphometric feature. While a full comparison between methods is beyond the scope of this paper, we note that the magnitude of group differences we detected (Table 2.3) compare favorably with approximately $20-30\%$ for caudate and approximately $5-20\%$ for ventricles reported by Apostolova's et al. Possibly these differences are because the current method, by using ICA, can simultaneously isolate superimposed sources of structural variability. If some of these sources of variability relate to normal inter-subject variability and some to PD-specific changes, then dissociating these sources of variability will enhance discriminatory power.

| ROI | L_CAU | L_PUT | L_THA | L_GLP | R_CAU | R_PUT | R_THA | R_GLP |
|---|---|---|---|---|---|---|---|---|
| Magnitude | 53.84% | 52.07% | 66.32% | 74.56% | 51.72% | 56.91% | 66.09% | 33.92% |

Table 2.3: The magnitude of significant between-group differences (in percentage).

## 2.5 Summary of contributions

We proposed a potential biomarker for PD. The marker is based on assessing the initial momentum of a diffeomorphic metric mapping from a template ROI to a given ROI. Using the initial momentum vector field as a feature, we found significant group different between PD and control subjects in basal ganglia ROIs. We also utilized ICA methods to decompose the initial momentum vector field seen across many subjects (Chapter 2), resulting in clinically meaningful components. Perhaps the greatest implication of this work is that it may be possible to perform cross-sectional studies on morphology. Usually the large inter-subject variability in anatomical structures makes it necessary to perform longitudinal studies and look for *differences* in morphology over time. With the current method, inter-subject variability is modeled as different loadings on fundamental deformation patterns – the ICs. Given that loading on many of the ICs had clinical significance, it may be possible to derive meaningful morphological information in a cross-sectional fashion.

To further validate this biomarker, it would be desirable to test the individual classification accuracy using initial momentum as a feature. The data will then be divided into training and testing groups, and classification accuracy will be tested over the permutation of training/testing assignment. As the initial momentum biomarker showed significant group differences, and significant correlations to the clinic scores, its classification accuracy is expected to be high. However, because the number of subjects whose data have been collected so far is limited, we leave this part for future work.

# Chapter 3

# Structural and SWI Image Joint Analysis

## 3.1 Background

Iron deposition in certain structures of the midbrain such as the substantia nigra (SN) and the red nucleus (RN), which can be imaged using the recently-developed susceptibility weighted imaging (SWI), is a potential biomarker for PD [71]. Because current registration methods which rely on whole-brain alignment do not provide good registration of the midbrain (e.g. see Chapter 1), studies investigating SWI of midbrain structures use manually segmented regions, and the mean voxel value within the ROI is then estimated and compared across subjects. However, studies have shown that degenerative changes in the SN in PD are not random, but rather follow a distinct spatial pattern so that cell loss is maximal in the caudal and mediolateral parts [34]. There are therefore benefits to accurate registration of midbrain structures.

The main challenge is accurate registration of SWI images to a template image, which then allows assessment of common spatial patterns of iron deposition. Traditional T1-weighted MR images alone are usually not sufficient for registration of midbrain structures due to its low intrinsic contrast, while SWI images do not offer adequate anatomical contrast except for possibly a few structures such as RN. Since neither T1 nor SWI images alone provide are suitable for mid-brain registration, we propose a hybrid "multi-structure" approach that jointly incorporates T1 images and manual binary segmentations of midbrain

structures in the SWI images concurrently into a non-rigid registration framework.

## 3.2 Methods

### 3.2.1 Data acquisition

The T1 and SWI images in this study are obtained on a 3 Tesla scanner equipped with a head-coil (3DT1TFE CLEAR, TR = 7.716ms, TE = 3.56ms, flip angle = 8, FOV = $256\times170\times200mm$). 19 PD subjects (15 male, 4 female, 17 right-handed, mean age=64 years, SD=9), and 18 age-matched normal control subjects are obtained. The RN (left and right) and midbrain areas are then manually segmented respectively on SWI images (magnitude maps) and T1 images by two trained raters using Amira 3D Visualization software (V.3.1.1.). The left and right ventral diencephalon (VDC) areas are segmented on original T1 images by Freesurfer [40] (shown together in Figure 3.1).

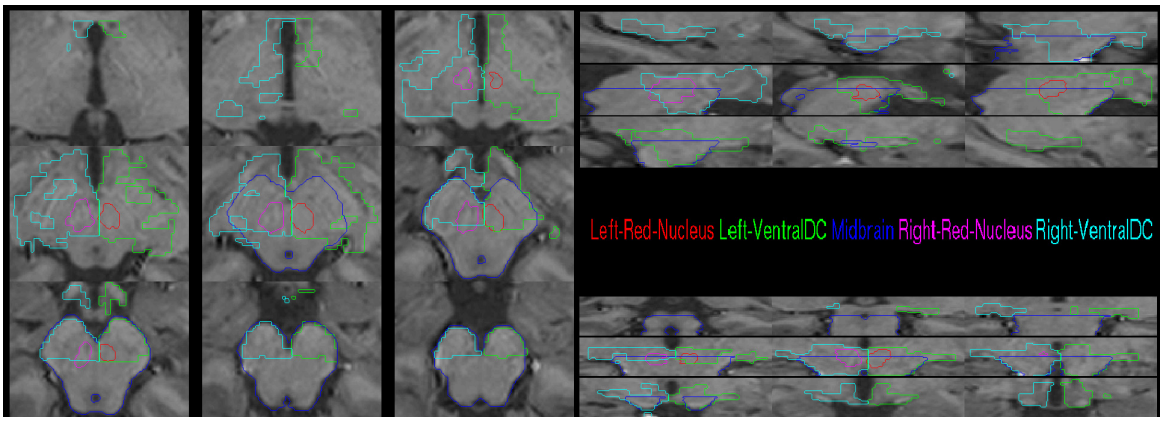


Figure 3.1: Outlines of midbrain areas (blue), left and right red nucleus (red and pink), left and right VDC areas (green and cyan) on T1 structural image. The 3x3 image array at left is Transverse view, the array in the upper right is Saggital view, and the lower right is Coronal view.

### 3.2.2 Registration algorithms

The registration algorithms contains three general steps. First, whole brain T1 structural images are registered to midbrain SWI images of same subjects with FLIRT (FMRIB's

Linear Image Registration Tool V.5.5). The 3D affine registration was applied to initially align the midbrain areas on T1 and SWI images, using Mutual Information [30][102] for the cost function. The same transformation is then applied on the binary segmentation of VDC and RN (both left and right) to align them to the SWI midbrain images.

Second, a 3D boundary box of $138 \times 126 \times 30$ voxels is cropped on the SWI images, including midbrain, RN and VDC areas. The size of the boundary box is chosen to include the ROIs in images of all subjects. The location of the boundary box in each SWI image depends on the location of midbrain. The size of the boundary box is set to include all the ROIs to be used as structures in the LDDMM. By performing the next step – the multi-structure registration – on the cropped SWI images, the computation expense can be significantly reduced.

Finally, we used a multi-structure diffeomorphic registration algorithm to register the SWI images (both magnitude and phase maps) within the boundary box to a common template. Diffeomorphic registration ensures the resulting transformations are one to one, invertible and smooth, and preserves the topological properties of the underlying anatomy [26]. Khan et al. [61] extended the existing single channel LDDMM [8] cost toward a multi-structure cost by inducing extra terms in the cost function for the mismatch of labeled ROIs.

Let the diffeomorphic transformation from target image $A$ to template image $B$ be $\varphi : \Omega \to \Omega$ such that $A \circ \varphi^{-1} \approx B$. The transformation $\varphi$ is based on the flow of smooth time-dependent velocity vector field $v_t \in V, t \in [0, 1]$ where $V$ is a Hilbert space of smooth, compactly supported vector fields on $\Omega$. The evolution function of a curve $\phi_{0,t}, t \in [0, 1]$ is defined by $\dot{\phi}_{0,t} = v_t(\phi_{0,t})$ such that the end point $\phi_{0,1}$ of the curve $\phi$ at time $t = 1$ is the particular transformation $\varphi = \phi_{0,1}$ that is sought for registration. Let $\phi_{s,t} : \Omega \to \Omega$ denote the composition $\phi_{s,t} = \phi_t \circ (\phi_s)^{-1}$ with the interpretation that $\phi_{s,t}(y)$ is the position at time $t$ of a particle that is at position $y$ at time $s$. Hence, the transformed image $A$ is given by $A \circ \varphi^{-1} = A \circ \phi_{1,0} \approx B$ and the transformed target image is $B \circ \phi_{0,1}$. The cost function for single channel LDDMM can be written as:

$$E(v) = \int_0^1 \|v_t\|_V^2 \mathrm{d}t + \lambda \|A \circ \phi_{1,0} - B\|_{L^2}^2 \tag{3.1}$$

Now let $A^{Seg,i}, i \in [1, \ldots, N]$ and $B^{Seg,i}, i \in [1, \ldots, N]$ be the $N$ binary segmentations on image $A$ and $B$ respectively. The sum of squares error terms in the cost function above can be

extended to simultaneously accommodate several structures contributing to the registration:

$$E(v) = \int_0^1 \|v_t\|_V^2 \mathrm{d}t + \lambda \|A \circ \phi_{1,0} - B\|_{L^2}^2 + \sum_{i=1}^{N} \lambda^{Seg,i} \|A^{Seg,i} \circ \phi_{1,0} - B^{Seg,i}\|_{L^2}^2 \tag{3.2}$$

In our study, the manual binary segmentation of midbrain, RN and VDC (left and right) are used as structure-channels (i.e. $A^{Seg,i}$ and $B^{Seg,i}$), as illustrated in Figure 3.2.

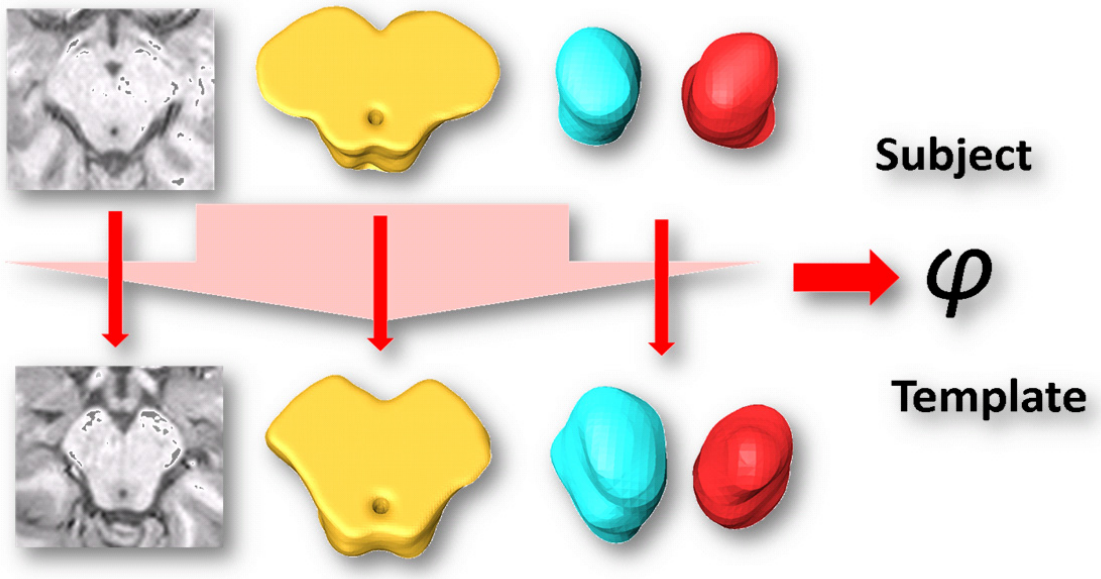


Figure 3.2: Illustration of the mechanism of multi-structure LDDMM. As binary segmentations of multiple structures are included, the optimal transformation can provide accurate mapping not only between whole brain images, but also between local structures.

## 3.3 Results

The results of the proposed multi-structure LDDMM method for registration with different structures are shown in Figure 3.3. The alignment improvement of RN and VDC areas can be seen after they are included as channels for the LDDMM registration.

Registration results of 5 PD and 5 control subjects, with both T1 images and binary

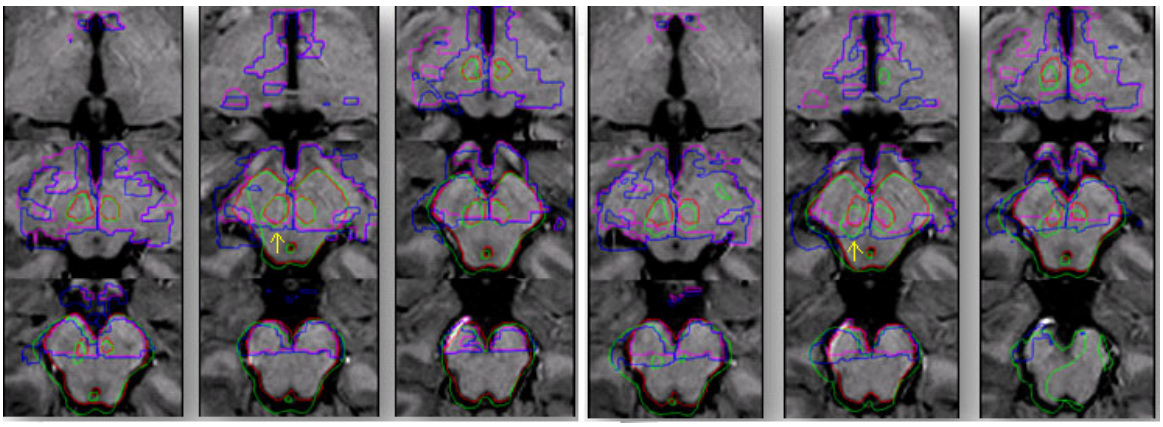

Figure 3.3: Compare of traditional and multi-structure LDDMM registration. Outlines of registered midbrain (green), RN (green), VDC areas (blue) overlaying corresponding template areas (red and pink) on a T1 structural image. The left side is multi-structure LDDMM registration, using the T1 structural image and binary segmentation of midbrain, RN, and VDC areas as structures. The 3x3 image array the Transverse view. The right side is single channel LDDMM registration results using only the T1 images alone. The difference is most obvious in the middle slice, where the yellow arrows point at.

segmentation of midbrain areas included as channels are shown in Figure 3.3. For comparison to a typical processing approach, the affine registration of T1 images is also used to compute a transformation which is then used to map midbrain areas onto the template. The registered midbrain areas of the 5 PD and 5 control subjects are shown in Figure 3.3.

To quantify the registration accuracy, the group mean DSC, defined in Equation 1.2 in Chapter 1, is computed for the registration results of both LDDMM (using only T1 and midbrain structure) and affine methods. The mean DSCs are shown in Figure 3.6. For the midbrain using the proposed multi-structure registration mean DSC is 0.89 for PD subjects and 0.88 for control subjects. In contrast, using the standard affine MR registration, mean DSC is 0.76 for PD subjects and 0.73 for control subjects.

To test the gain of additional structures in multi-structure LDDMM algorithm, we computed the DSC of 5 different ROIs registered by LDDMM with following configurations:

0-structure: only T1 images are used.

1-structure: T1 images and binary segmentation of midbrain are used.

4-structure: T1 images and binary segmentation of midbrain and RN (left and right)

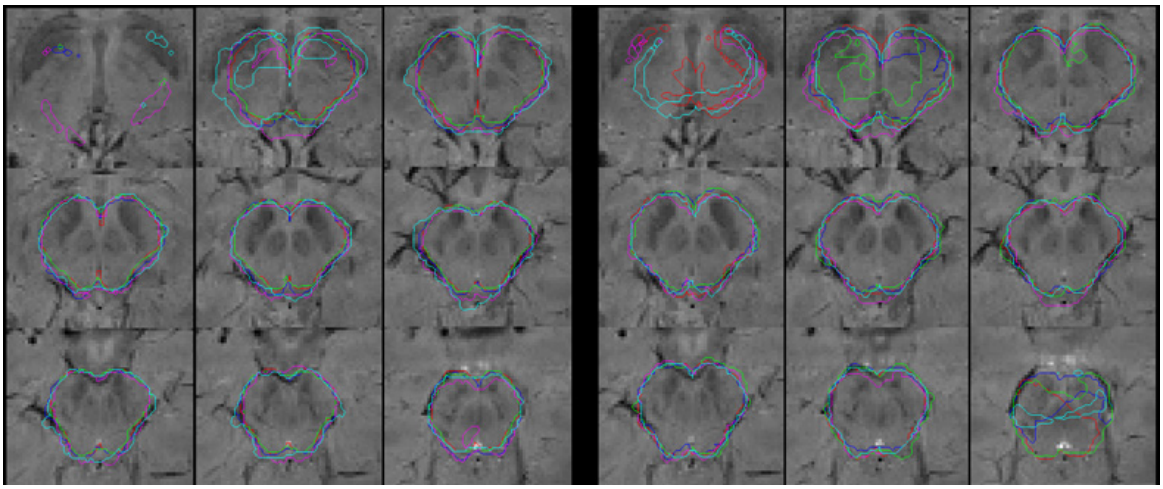

Figure 3.4: Alignment of 5 midbrains registered by multi-structure LDDMM. Outlines of midbrain areas registered by multi-structure LDDMM. In the left 3x3 image array the 5 outlines with different color represents 5 registered normal control midbrain areas (Saggital view). On the right are 5 registered PD midbrain areas. Note the right below slice is the bottom of midbrain that is not always parallel with slicing direction after registration, hence the low overlap.

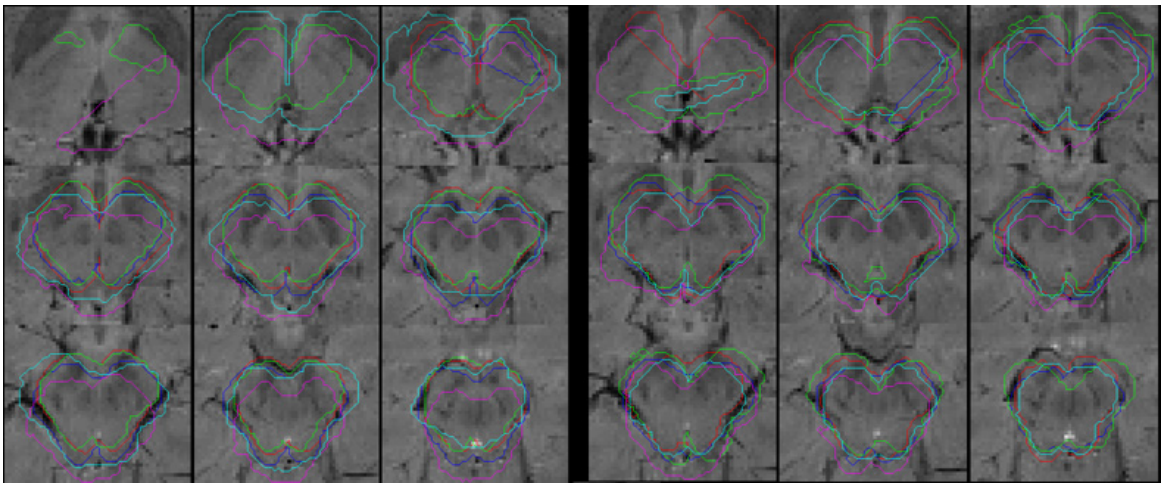

Figure 3.5: Alignment of 5 midbrains by affine registration. Outlines of midbrain areas registered by affine registration. In the left 3x3 image array the 5 outlines with different color represents 5 registered normal control midbrain areas (Saggital view). On the right are 5 registered PD midbrain areas. Note the right below slice is the bottom of midbrain that is not always parallel with slicing direction after registration, hence the low overlap.

are used.

6-structure: T1 images and binary segmentation of midbrain, RN and VDC (left and right) are used.

The average DSCs of registration results under above configurations are shown in Table 3.1. From the table we can see the matching of the corresponding structures is improved with multi-structure registration as they are included. Specifically, using the manual midbrain binary segmentation concurrently with T1 weighted MR image adds errors in midbrain matching to the error term directly, and thus provides better overall midbrain matching. Adding the mismatch of the binary segmentations of the red nucleus into the error term further refines the non-linear transformation. One important aspect to note is that unlike binary-segmentation matching only, the concurrent use of T1 MR images also provides texture information inside the segmentations thereby providing better anatomical registration within the ROI. This is important for registration within multi-compartment and anatomically complex areas such as the midbrain.

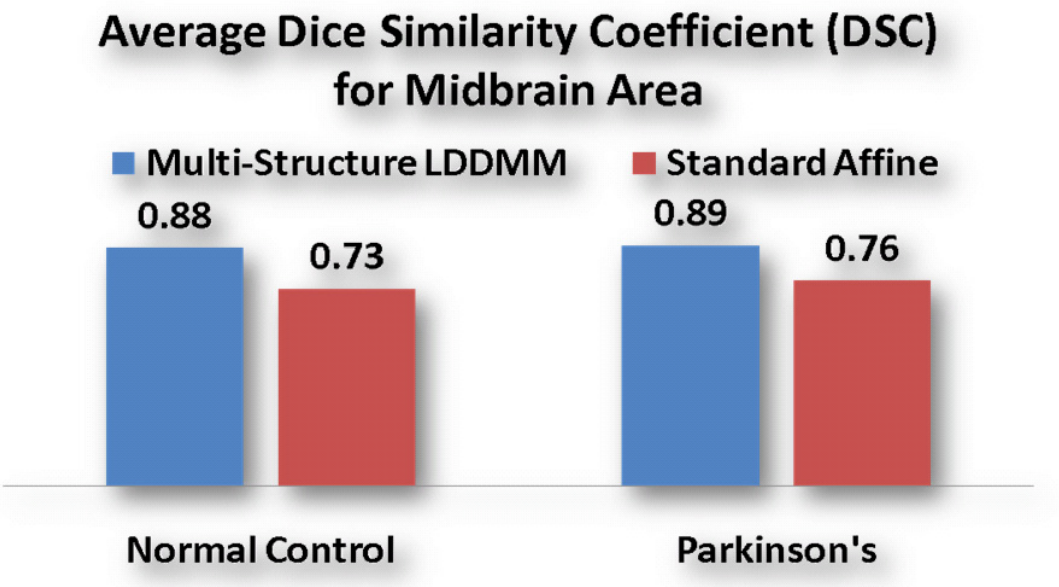


Figure 3.6: Average DSCs for LDDMM and Affine registration results.

Table 3.1: Average DSCs of registered ROIs with different multi-structure configurations.

| Structure No. | Midbrain | Left RN | Right RN | Left VDC | Right VDC |
|---|---|---|---|---|---|
| 0 | 0.79 | 0.58 | 0.56 | 0.59 | 0.60 |
| 1 | 0.87 | 0.71 | 0.73 | 0.77 | 0.79 |
| 4 | 0.91 | 0.83 | 0.85 | 0.83 | 0.86 |
| 6 | 0.91 | 0.84 | 0.85 | 0.86 | 0.87 |

To interpret the anatomical meaning of the outputs of our proposed methods, we computed the optimized transformation with multi-structure LDDMM (4-structure configuration), and applied on SWI images (magnitude maps). We then measured the voxel-wise group difference between PD and control subjects on the registered SWI images. A two-sample T-test function in Matlab (Oct 20, 2005: v1.22) was implemented. We use RFDR (defined by Equation 2.6 in Chapter 2) to correct the p-values threshold for multiple compare. The significant p-values (p<RFDR) on the template T1 background are shown in Figure 3.7. Clusters of voxels with significant group difference can be seen on the figure. A closer look of one particular cluster is shown in Figure 3.8.

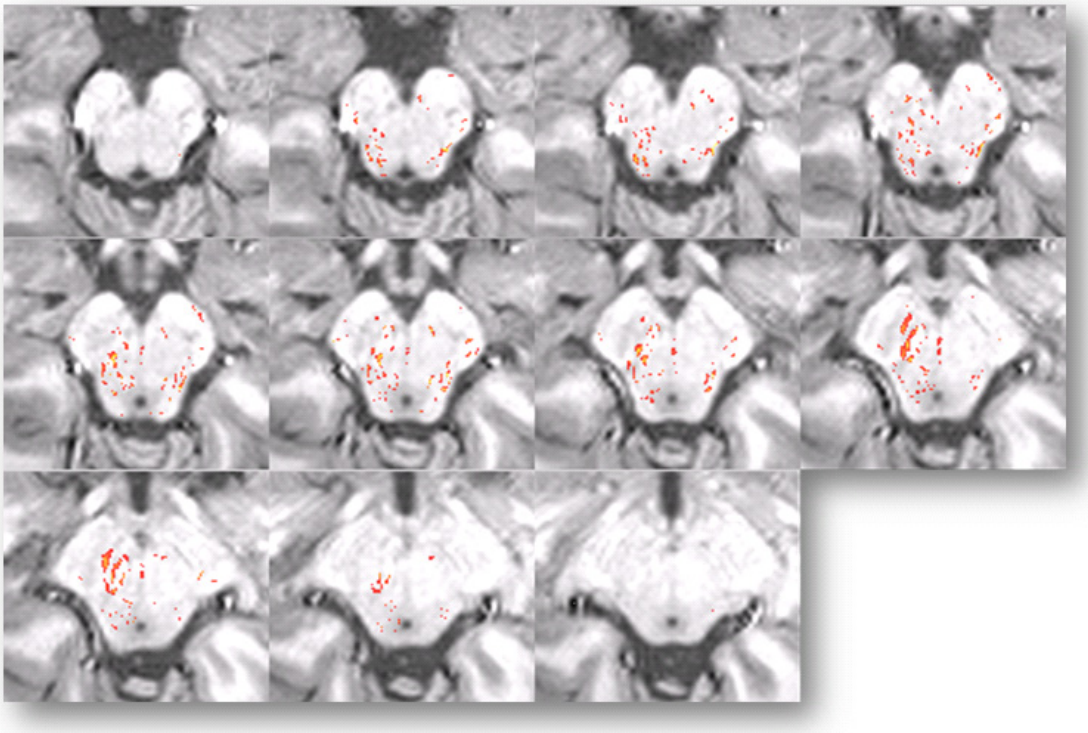

Figure 3.7: Cluster of significant group difference on registered SWI images. 9 slices of SWI magnitude maps (Axial view) are displayed. The red area represents the location where significant group difference of iron content is detected.

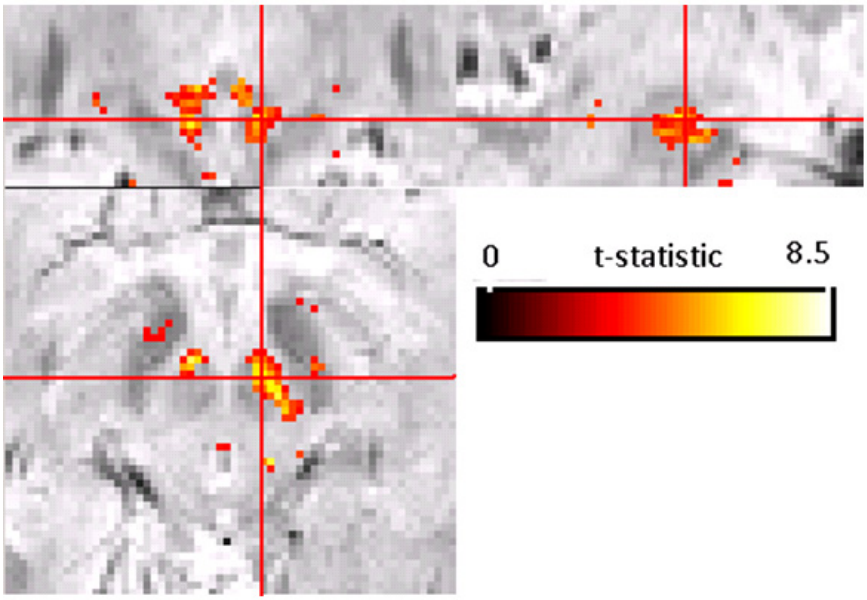


Figure 3.8: Closer look of one particular cluster of significant group difference on registered SWI images, located by the red cross lines. Up left is Coronal view, up right is Sagittal view, and down left is Axial view.

## 3.4 Summary of Contributions

We developed a new method of multi-structure LDDMM registration and analysis of SWI data. The proposed method uses multiple concurrent streams of anatomical information for the registration of complex brain areas such as the mid-brain. Experiments demonstrate that, for both PD and control subjects, the multi-structure LDDMM method, by incorporating binary segmentations of areas such as the RN and VDC, improved alignment of structures on, within, and near midbrain areas, thus providing more reliable registration of SWI images for localizing group difference of midbrain iron content.

# Chapter 4

# Structural and DTI Image Joint Analysis

## 4.1 Background

Brain morphometry, i.e. quantification of gross anatomical features often derived from non-invasive medical imaging procedures, is increasingly important in the assessment of brain disease. Traditionally, trained radiologists have scrutinized brain images (e.g. CT, MRI) for pathological processes such as stroke, tumor, abscess, etc., with little regard for morphological changes. In some neurodegenerative conditions such as Alzheimer's disease, there can be sufficient widespread atrophy that it is apparent by gross inspection. However, in diseases such as Parkinson's Disease (PD), the second most common neurodegenerative disorder after Alzheimer's disease (affecting approximately 1% of the population above the age of 65), morphological changes are typically not obvious, even to the trained eye. Thus quantifiable methods are required to determine if robust changes in structure exist in PD.

Voxel-based brain morphometry (VBM) is the most common brain morphometry analysis method. In VBM, subject brain images are typically registered to a common template image, and statistical analysis is performed on a voxel-by-voxel basis on the registered subject brain images. Previous VBM studies on gray matter structures have reported significant changes in PD subjects [18] [58] [75]. However, VBM depends heavily on accurate registration [14], which is problematic in disease populations as focal atrophy of some brain

structures may lead to spatially specific misregistration despite optimization of a cost function that encompasses whole-brain alignment (Chapter 1).

Besides structural T1-weighted images, other MRI techniques have been proposed for exploring microstructural changes, particularly in the white matter. One such technique is diffusion tensor imaging (DTI), where linearly-varied pulsed field gradients are used to estimate water diffusivity in different directions to provide a tensor of estimated diffusivity at each voxel position. While it is difficult to provide a direct mapping between the diffusivity results and the underlying pathology, the mean diffusivity increases with extracellular fluid accumulation, and the fractional anisotropy provides information on the microstructural integrity of highly oriented microstructures such as white matter tracts [1]. Both mean diffusivity and fractional anisotropy are highly influenced by physiological aging [25]. FA changes have been frequently described in PD. Reduced FA values in the substantia nigra (SN), the site of primary neurodegeneration in PD, have been demonstrated in a cross-sectional study of 73 PD patients and 78 age matched controls [21], and in a smaller study of 14 untreated PD and 14 age- and gender-matched controls [99]. However, decreased FA values in PD have been reported in a number of other brain regions, including the frontal lobes [59], the genu of the corpus callosum [45] and in the superior longitudinal fasciculus [45] and near the gyrus rectus [57]. Furthermore PD subjects with associated depression have reduced FA values in the medial dorsal thalamus, with the changes correlating negatively with the severity of depression [69].

Since VBM results are critically dependent upon proper registration [14], it reasonable to assume that significant DTI changes reported in disease states [86] [15] – which also include registration as part of the processing steps – may also be significantly dependent upon accurate registration. This may be particularly relevant in the assessment of neurodegenerative diseases, such as Alzheimer's or PD.A quick inspection of the voxel-wise intensity variance of registered T1 and ADC maps, as shown in Figure 4.1, suggests that qualitatively they are very similar, raising the question as to how much of previously-reported DTI variability may be on the basis of subtle misregistration, as opposed to actual changes in DTI parameters. In fact, misregistrations are often spatially-dependent, as shown in Figure 4.1, which means some locations are better registered than others just by the morphology of the neighborhood. Hence, any registration method that is employed to register anatomical structures and transform DTI data will likely transform non-homologous voxels on top of each other and lead to interpretation errors in DTI changes due to disease.

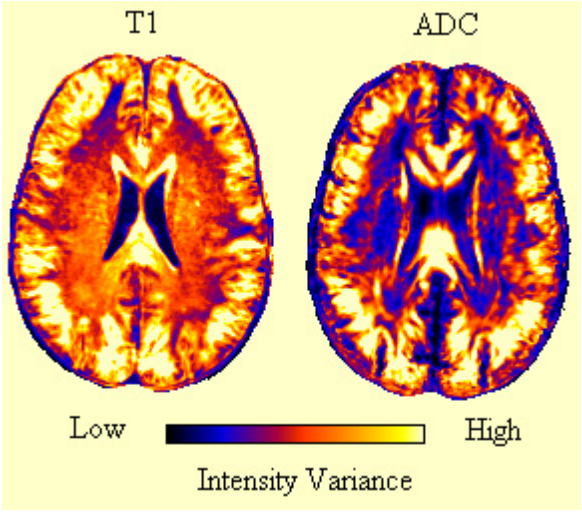


Figure 4.1: Voxel-wise intensity variance of co-registered T1 images and ADC maps computed from the same subjects DTI data. The same Axial view slice of both image modal are displayed, T1 on the left and ADC on the right. The bright yellow color represents high variance, and the dark blue color represents low variance.

Analyzing DTI data based on the assumption that the underlying anatomical data are perfectly registered may therefore be problematic. DTI data are usually assessed by examining the mean value of voxel parameters in certain regions, or by tractography. In tractography, the fractional anisotropic or FA values from a voxel and its neighbours are used to try and infer the dominant direction of white matter tracts, but this requires a number of assumptions especially when dealing with the potential of white matter tracts that may be intersecting [9]. One way to incorporate anatomical information and other imaging information from same subject is to simply concatenate the different modalities, thus forming a higher dimensional feature vector for each subject, as has been suggested for anatomical and fMRI data [19]. However, the physical meaning of the combined features is unclear in this method, especially after dimension reduction. Here we propose jointly examining anatomical and DTI data that have been registered to a common template and then using the Fukunaga-Koontz Transform [44] to jointly transform DTI maps and the associated T1-weighted images into common spatial components – albeit with complementary loadings. This allows selection of linear subspaces that are more sensitive to residual anatomical variation while being insensitive to DTI changes, and vice versa. We demonstrate that even

when a highly accurate registration method is used, such as Large Deformation Diffeomorphic Metric Mapping (LDDMM), significant changes in DTI maps previously reported in PD may in fact be largely on the basis of subtle differences in anatomical variability.

## 4.2 Methods

While fully elucidated below, in brief, DTI and T1 scans were collected from both PD and controls subjects and then co-registered to a group average template using a combination of affine registration and LDDMM registration. The FKT was then performed to compute a joint space of anatomical and DTI data from the co-registered scans. Linear subspaces emphasizing variability in anatomy (i.e. T1) or variability in DTI were selected. Finally Independent Component Analysis (ICA) was applied to extract spatial patterns in the different subspaces. The loadings of the independent components (ICs) across subjects were then examined to assess their ability to discriminate between PD and normal subjects.

### 4.2.1 Data acquisition

Data were collected from 16 PD subjects and 21 age-matched controls. Subjects were scanned using a Philips Achieva 3.0 T scanner (Philips, Best, The Netherlands), with an 8-channel head coil. A "memory foam" pillow was used to minimize head motion. For collection of the DWI images the following parameters were used: 60 axial slices, repetition time 6000-7000 ms, echo time 69 ms, flip angle 90 degrees, FOV $212 \times 212$ mm, acquisition matrix size $96 \times 95$, pixel size $0.8281 \times 0.8281 \times 2.200$ mm with no gap. Thirty-two independent directions, with a b-value of 700 $s/mm^2$, scan duration 200-250 sec. A reference image with no diffusion weighting was also obtained. Three separate DWI scans with identical parameters were performed and results averaged to increase the signal-to-noise ratio.

We also obtained T1 weighted images with the following parameters: 170 axial slices, repetition time = 7.7 ms, echo time = 3.6 ms, flip angle 8 degrees, field of view $256 \times 200$ mm, acquired matrix size $256 \times 200$, and pixel size $1 \times 1 \times 1$ mm.

The initial .PAR/.REC files were first converted to Analyze format using the freeware program dcm2nii [13] [78]. The images from the three separate acquisitions were then averaged. Gradient tables were extracted using the freeware program "DTI gradient table creator" [65] [28] with the following parameter settings "didREG - n"; "grad choice - yes-ovp-high"; "fat hift - P"; "sort images - y". For "release" we used either "Rel 2.1" or "Rel

2.5" depending upon the date of scan acquisition.

### 4.2.2 Co-registration

The DTI and T1 scans were registered to a common template (described below) using a combination of affine registration and high dimensional non-linear registration. First the FA and ADC maps were co-registered to the T1 scans using the within-subject co-registration module of Statistical Parametric Mapping [6], which uses a 12-parameter affine transformation matrix with a normalised mutual information cost function [93]. For the non-rigid registration inter-subject registration, we used a multi-structure diffeomorphic registration algorithm, employing corresponding structure labels (both subcortical and cortical) to guide and constrain the high-dimensional registration [61].

The open source Freesurfer image analysis suite [40] was used to the generate subcortical segmentations and cortical parcellations making up the multi-structure image set, resulting in the cost function shown in Equation 3.2 (Chapter 3). We used the following 8 subcortical structures (both left and right) to guide the registration: lateral ventricles, caudate nucleus, putamen, pallidum, nucleus accumbens, thalamus, hippocampus, and amygdala.

For cortical structures, we used the following 34 labels (both left and right): banks around the superior temporal sulcus, caudal anterior cingulate, caudal middle frontal, corpus callosum, cuneus, entorhinal, fusiform, inferior parietal, inferior temporal, isthmus cingulate, lateral occipital, lateral orbito-frontal, lingual, medial orbito-frontal, middle temporal, parahippocampal, paracentral, pars opercularis, pars orbitalis, pars triangularis, pericalcarine, postcentral, posterior cingulate, precentral, rostral anterior cingulate, rostral middle frontal, superior frontal, superior parietal, superior temporal, supramarginal, frontal pole, temporal pole, and transverse temporal. Including the MRI as the first structure, we therefore have 43 structure-channels for each hemisphere making up the multi-structure set. For the sake of efficiency the implementation used a locally-optimal solution to the variational problem, as described in [27].

The choice of common template can affect registration accuracy and introduce bias. We therefore selected a "typical" scan from the pool of available scans to act as the template. The "typical" scan was selected by iteratively generating a groupwise average by 1) estimating the average using a voxel-wise average of the registered subjects, and 2) computing pairwise registration of each subject to the newly estimated average [60]. The initial template was one of the control subjects and the initial registration used a low-dimensional

affine registration. A multi-scale smoothing schedule was also used with initial iterations of the diffeomorphic registration constrained to a high degree of smoothness, then decreased for successive iterations (4 total iterations). Groupwise registration of the entire dataset (37 subjects) took 52 hours using a 400-core computing cluster, with each pairwise registration running in approximately 2 hours on a single core.

As a comparison, we also applied the commonly-used Statistical Parametric Mapping method (SPM5, by Wellcome Dept. of Imaging Neuroscience, 2005)) for T1-to-T1 registration. The spatial normalization module with default setting was used to register the T1 scans to the same group average template that was used with the LDDMM registration program. Each SPM pairwise registration runs in approximately 10 minutes for on a single core.

Once the T1-to-T1 transformation was computed for each subject, the DTI scans which had previously been co-registered to the T1 scans were further transformed to the template space using the same transformation parameters computed from the T1-to-T1 registrations. Data from all subjects (16 PD and 21 age-matched 21 Controls) were all registered to the same template for subsequent analysis.

### 4.2.3 Fukunaga-Koontz Transform

The Fukunaga-Koontz Transform (FKT) is a classic feature selection method invented in 1970 for image analysis [44]. The basic assumption of FKT is similar to Quadratic Discriminant Analysis (QDA), where the distributions of two classes are multivariate normal. In fact, under certain condition, FKT is the "optimal" low-rank approximation to the QDA [66]. The advantage of FKT over Linear Discriminant Analysis (LDA) (or the Fisher analysis) is it has no assumption of equal variance/covariance matrices for the two classes. Therefore it can still be effective to those data LDA fails to classify.

The FKT can be jointly applied to the DTI and anatomical data as follows. Let $x_i \in X$ denote the set of anatomical T1 images, and $y_i \in Y$ denote the set of DTI images. We first place the voxel values of each 3D image into a long column vector. Because the anatomical and functional images are co-registered and the images are all of the same resolution, the vectors are of same length. Without ambiguity, let $x_i$ and $y_i$ denote the set of vectors of anatomical and functional images respectively, with group mean subtracted. Let $\Sigma_x = E(x_i {x_i}')$ and $\Sigma_y = E(y_i {y_i}')$, $\Sigma_x + \Sigma_y$ is then positive semi-definite and can be decomposed as $\Sigma_x + \Sigma_y = \Phi D \Phi'$, where $\Phi$ is the matrix of eigenvectors of $\Sigma_x + \Sigma_y$, and $D$ is a diagonal

matrix of eigenvalues. Let $P = \Phi D^{-1/2}$, and $\tilde{x}_i = P'x_i$, $\tilde{y}_i = P'y_i$, then we have

$$P'(\Sigma_x + \Sigma_y)P = I \tag{4.1}$$

The covariance matrices for the transformed data $\tilde{x}_i$ and $\tilde{y}_i$ are $C_{\tilde{x}} = P'\Sigma_x P$ and $C_{\tilde{y}} = P'\Sigma_y P$. From Equation 4.1 we have $C_{\tilde{x}} + C_{\tilde{y}} = I$. This means the covariance matrices of the transformed data $\tilde{x}_i$ and $\tilde{y}_i$ have the same eigenvectors, and the sum of their eigenvalues associated with the same eigenvector is always equal to 1. To prove this, let $z$ be an eigenvector of $C_{\tilde{x}}$, associated with eigenvalue $\lambda$, i.e. $C_{\tilde{x}}z = \lambda z$. Then we have $(C_{\tilde{x}} + C_{\tilde{y}})z = C_{\tilde{x}}z + C_{\tilde{y}}z = \lambda z + C_{\tilde{y}}z$. On the other hand since $C_{\tilde{x}} + C_{\tilde{y}} = I$, we have $(C_{\tilde{x}} + C_{\tilde{y}})z = I \times z = z$ Therefore $\lambda z + C_{\tilde{y}}z = z$, and $C_{\tilde{y}}z = (1 - \lambda)z$, which means $z$ is also an eigenvector of $C_{\tilde{y}}$, associated with eigenvalue $1 - \lambda$.

Because of the above property, the "dominant eigenvectors" of $C_{\tilde{x}}$, which have large eigenvalues of $C_{\tilde{x}}$, will have small eigenvalues of $C_{\tilde{y}}$, which makes them the "weak eigenvectors" of $C_{\tilde{y}}$. Therefore, the projection of original image vectors on the first several dominant eigenvectors represent maximal anatomical variability (information), and minimal DTI variability (information), and vice versa. This property of the FKT allows us to select linear subspaces that are relatively anatomical-prominent or DTI-prominent.

In our study, as the dimension of image vector is extremely high (over 10 million), computing the covariance matrices of $\Sigma_x = E(x_i x_i{}')$ and $\Sigma_y = E(y_i y_i{}')$ and eigen-decompose them can be very expensive in computation. However the number of image vectors is relatively small (less than 40). Therefore one way to reduce computational complexity of FKT is to eigen-decompose $\Sigma_{x'} = E(x_i{}' x_i)$ instead of $\Sigma_x = E(x_i x_i{}')$. Let $v$ be an eigenvector of $\Sigma_{x'}$, and $u$ be an eigenvector of $\Sigma_x$, we can compute $u$ by $u = Xv$.

### 4.2.4 Selection of linear subspaces

Let $S = [s_1 s_2 ... s_n]$ be the matrix formed by the eigenvectors of $C_y$, ranked in the descending order of associated eigenvalues. The $s_i$ can be regarded as a basis emphasizing the DTI variability in $y_i$. By choosing a subset containing the first $m$ eigenvectors, $S_m = [s_1 s_2 ... s_m]$, we can project $y_i$ onto a subspace most representing the DTI variability and least representing the anatomical variability at the same time. Note that since the column vectors $x_i$ and $y_i$ correspond to the same subjects, the projected vectors $\widehat{y_i} = S_m y_i$ also correspond to the same subjects.

The eigenspectrum for covariance matrices $C_y$ (also for $C_x$ because of equation 4.1) is shown in Figure 4.2 (see Results). Since it was noted that the anatomical variation was restricted to the last 3 eigenvectors and DTI variation was largely restricted to the first 7 eigenvectors, we chose following linear subspaces to test the dependency of DTI variability on anatomical difference:

1. Total subspace: $S_1 = [s_1 s_2 ... s_n] = S$. All eigenvectors are selected. The subspace is equal to the whole space. Therefore no concentration on DTI or anatomical variability are applied, and this is the typical scenario.

2. T1-weighted subspace: $S_2 = [s_8 s_9 ... s_n]$. The 7 eigenvectors representing largely DTI variability are removed. The subspace spanned by the rest of the eigenvectors represents approximately 80% variability on DTI data that is MORE dependent on anatomical difference.

3. DTI-weighted subspace: $S_3 = [s_1 s_2 ... s_{n-3}]$. The 3 eigenvectors representing largely T1 variability are removed. The subspace spanned by the rest of the eigenvectors represents approximately 90% variability on DTI data that is LESS dependent on anatomical difference.

4. DTI-concentrated subspace: $S_4 = [s_1 s_2 ... s_7]$. Only the 7 eigenvectors representing most DTI variability are kept. This subspace concentrates on DTI variability while contain approximately 20% variability on DTI data that is most independent on anatomical difference.

### 4.2.5 Independent Component Analysis (ICA) on linear subspaces

We used ICA to find linear independent spatial patterns within the subspaces defined above. ICA decomposes the $\widehat{y_i}$ into a mixing matrix $A$ and independent components $c$ so that $\widehat{Y} = Ac$, where the rows of $\widehat{Y}$ corresponds to $\widehat{y_i}'$ and the rows of matrix $c$ are maximally linearly independent. Because of the stochastic nature of the learning process, the computed ICs can vary slightly from different session to session, particularly if they represent a small amount of the original variance. One approach to deal with this problem is to perform repeated analysis on the same data set with different initiation values, and check for the consistency of the extracted components. We used the ICASSO package for Matlab (Oct 20, 2005: v1.22) to concentrate on ICs that were robust to changes in initial conditions. We only examined ICs whose "estimated stability index" from the ICASSO exceeded 0.8.

Separate ICA analyses were performed on the different subspaces and DTI maps (i.e. three subspaces $\times$ two maps = six analyses). The columns of $A$ represent the loadings of

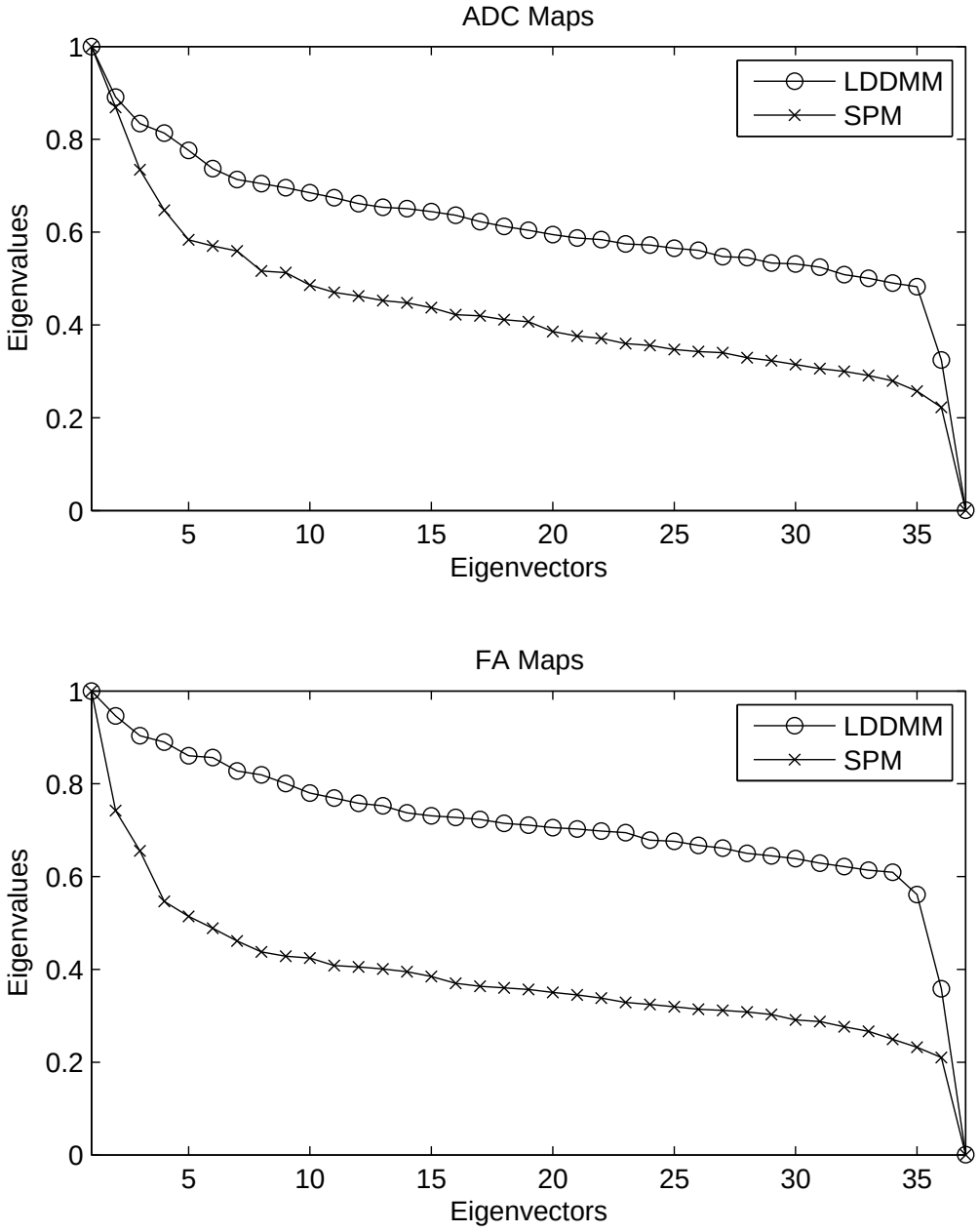


Figure 4.2: Eigenspectrum of the covariance matrices for Fukunaga-Koontz transformed FA and ADC data. Both LDDMM-registered and SPM-registered data are displayed. The eigenvalues are arranged in descending order. The eigenvectors of covariance matrix of the transformed LDDMM-registered data have higher eigenvalues than the SPM-registered data in general, and for the LDDMM-registered data the eigenvalues decrease slower than the SPM-registered as the eigenvectors become more and more concentrated on anatomical variability.

the corresponding spatial pattern given in $c$. In order to assess if the spatial pattern $c_i$ was expressed differently between PD and controls, we performed a t-test on loading between PD subjects and normal controls on the corresponding column of $A$. We corrected for multiple comparisons by using the False Discovery Rate approach.

## 4.3 Results

We computed T-statistic of significant group difference with the Matlab toolbox SurfStat (Keith J. Worsley 2008). For each subspace the numbers of voxel with significant group difference (normalized by the percentage of variability represented in each subspace) are shown in Figure 4.3. For both FA and ADC data, there is progressive reduction in group differences as the subspace concentrated more on DTI variability from T1 variability. SPM generally detected more voxels with significant group difference than LDDMM. This is likely because is a higher dimensional registration approach is implemented in LDDMM, resulting in less anatomical variability in the registered data.

For the six ICA analyses (Total, T1-weighted and DTI-weighted subspaces for SPM and LDDMM registered data), we performed the two sample t-test on the IC loadings for each analysis. Figure 4.4 demonstrates the number of ICs in each analysis whose loadings are significantly different between PD and control subjects (denoted as "significant ICs"). The lowest p-values (representing the most significant group difference on IC loadings) of three analyses on LDDMM-registered data are listed in Table 4.1. Similar to the voxel results, significant ICs were found in both SPM-registered data than the LDDMM-registered data. However as the subspace became more DTI-weighted, the number of significant ICs become more similar between SPM and LDDMM. The IC with lowest p-values in DTI-weighted and T1-weighted subspaces are shown in Figure 4.5 and 4.6. The spatial patterns are different for those two ICs, with the DTI-weighted IC corresponding to the white matter deep to the surface of the primary motor cortex. In contrast, the T1-weighted significant IC was closer to the cortical surface.

In order to assess the potential discriminating benefit of isolating different subspaces, we first found the IC in the DTI-weighted subspace that had the highest discriminint value on its loadings (t = 2.9855, p=0.0051) and then determined the IC in the total subspace that best matched (by correlation) the DT-weighted subspace IC (r = 0.0887, p$\approx$0, note the length/dimension of IC is 1611899, therefore the highest correlation coefficient r is still

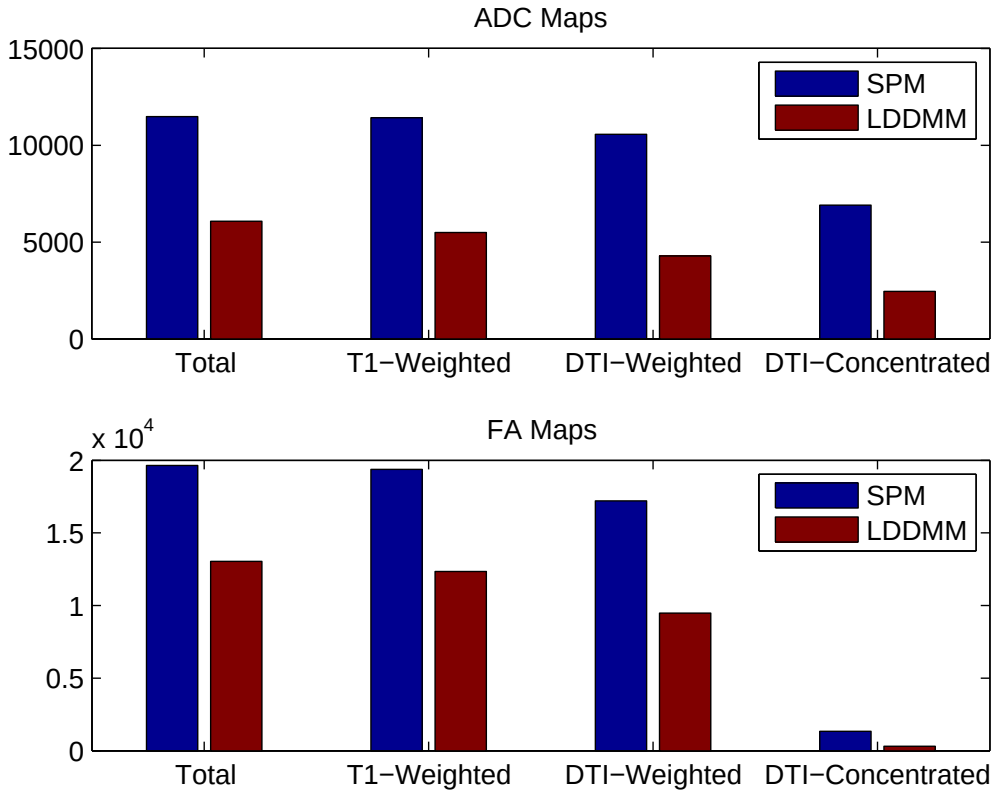


Figure 4.3: Number of voxels with significant group difference detected from ADC and FA maps within FKT-generated linear subspaces.

very low in absolute value). We then interrogated the loading of the total subspace IC to assess its dicriminability and noticed that it was less discriminating than the DTI-weighted IC (t=2.3024, p=0.0274).

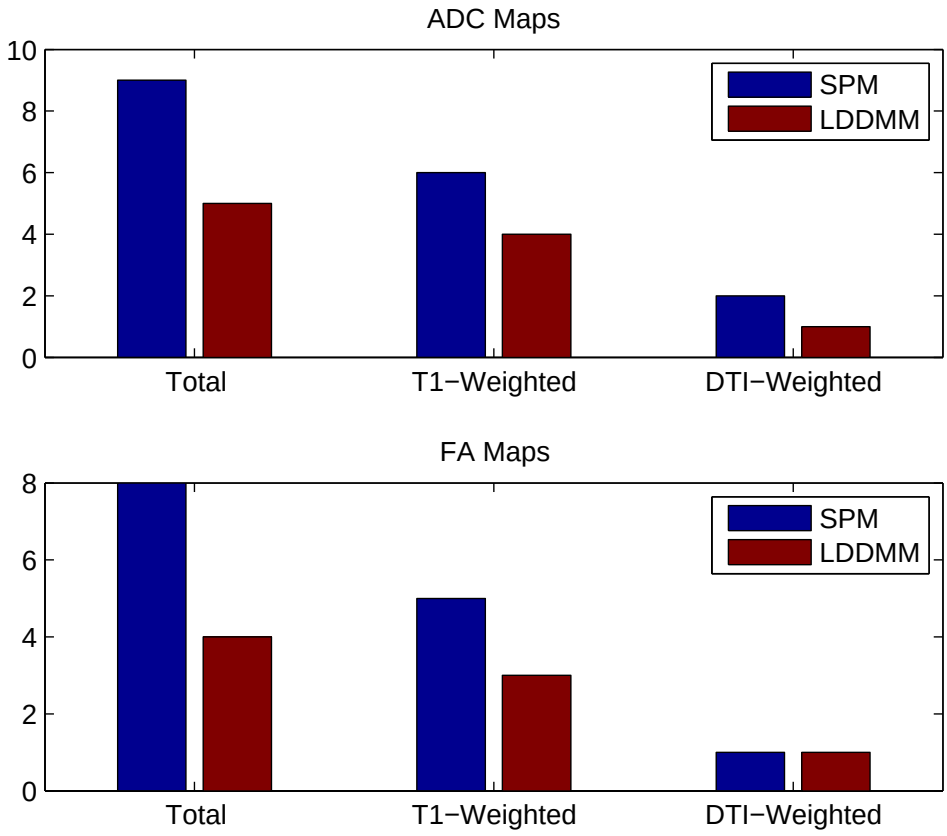


Figure 4.4: Number of ICs with significant different loadings between PD and control subjects detected from ADC and FA maps within FKT-generated linear subspaces.

## 4.4 Discussion

We have used the FKT to isolate differences in morphology from DTI changes in PD subjects with respect to normal controls. Our results suggest that subtle differences in morphology after registration tend to dominate, rather than changes in DTI parameters themselves 4.2.

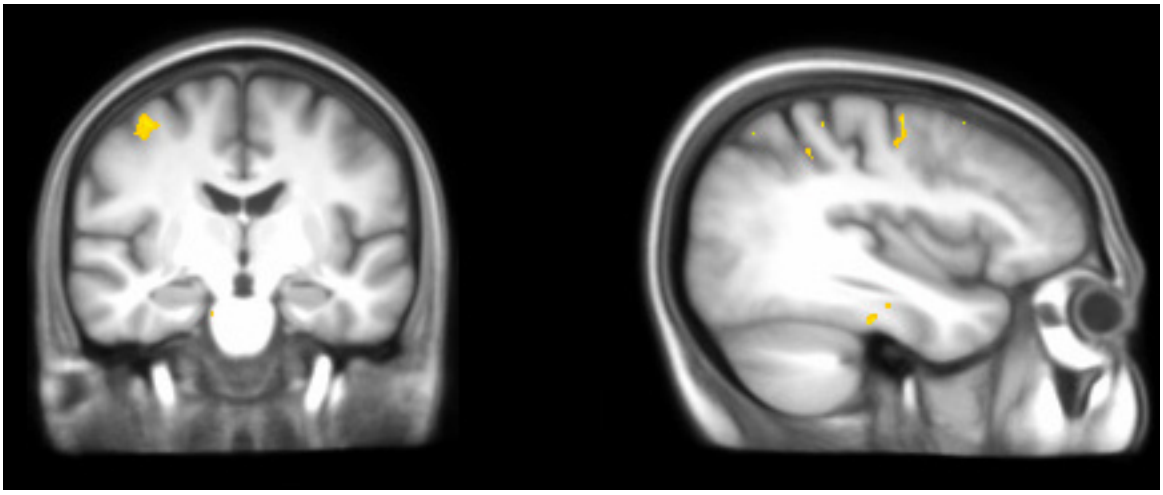

Figure 4.5: IC patterns of FA maps that loaded significantly differently between PD and control subjects, on the DTI-weighted subspace. Left slice is Coronal view, and right slice is Sagittal view.

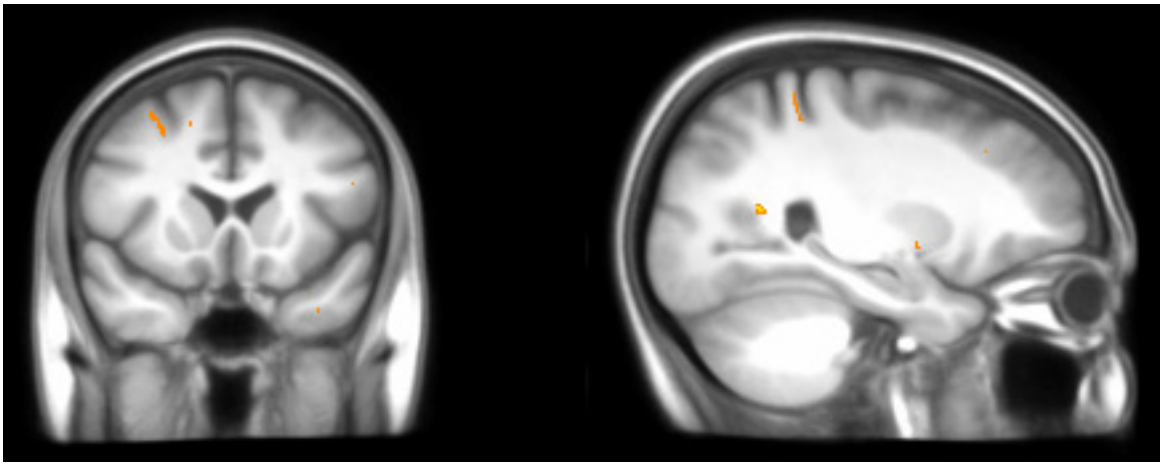

Figure 4.6: IC patterns of FA maps that loaded significantly differently between PD and control subjects, on the T1-weighted subspace. Left slice is Coronal view, and right slice is Sagittal view. Different slices are shown for the DTI-weighted and T1-weighted subspaces because the different location of the respective IC patterns.

Table 4.1: P-values of two sample T-tests on IC loadings

| | Total | T1-Weighted | DTI-Weighted |
|---|---|---|---|
| ADC | 0.0237 | 0.0118 | 0.0071 |
| FA | 0.0244 | 0.0196 | 0.0051 |

The eigenspectrum shows the eigenvectors of covariance matrix of the transformed LDDMM-registered data have higher eigenvalues than the SPM-registered data in general, and for the LDDMM-registered data the eigenvalues decrease slower than the SPM-registered as the eigenvectors become more and more concentrated on anatomical variability. This may indicate that LDDMM registered data contains less anatomical variability and more DTI variability, as would be expected with a higher-dimension registration process.

Changes in morphology have been previously described in PD, although they tend to be subtle. Studies that have looked at the overall volume of structures have tended not to show significant changes [2]. However, newer analytical methods that allow assessment of the shape have demonstrated shape changes in the thalamus are apparent in non-demented PD subjects, even when the overall volume of the thalami was not significantly different between PD subjects and controls [72]. While the morphological changes detected here may ultimately prove diagnostically and/or prognostically useful, the results must be interpreted with caution. The ICA model, when applied to the anatomically weighted subspaces, assumes that the images can be accurately modelled as a linear superposition of (spatially) independent patterns. The spatially independent patterns are assumed stationary and non-deformable. So a pattern that differentiates PD from normal subjects will tend to load heavily on voxels to create spatial patterns around structures such as the ventricle and the sulci (as shown in Figure 4.7). Similar to VBM, such a pattern does not automatically infer atrophy of say, peri-ventricular structures, as it may represent changes in overall ventricular volume or other medial structures but when superimposed, the changes in peri-ventricular structures are most apparent. We note that asymmetric ventricular enlargement has been previously described in PD [68].

Our results further suggest that previously reported DTI changes in PD (and in many other situations as well) that assume perfect anatomical registration may need to be interpreted with caution. It is possible that the differences we observed were due to the registration process we used. However, we used a highly accurate multi-channel registration process that has been previously been shown to be accurate in PD [22] which would mitigate

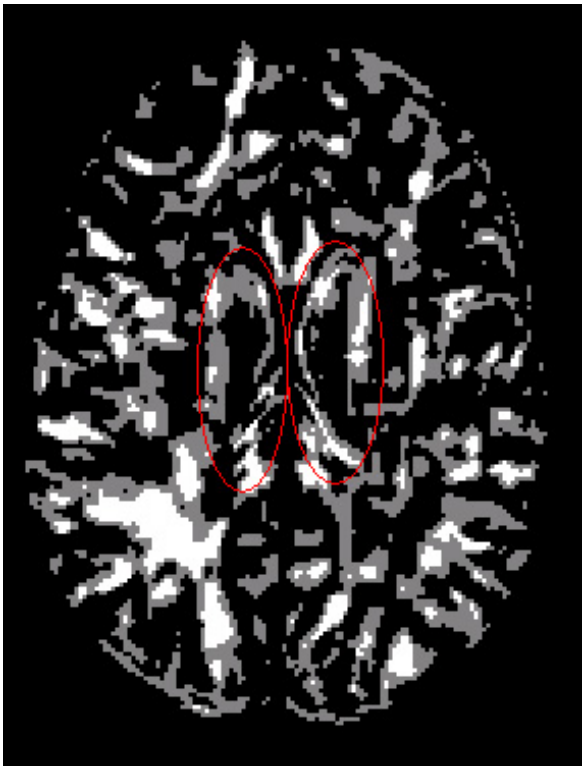

Figure 4.7: A typical PD-related independent component (IC) shown as spatial pattern in native brain space. An Axial view slice is displayed. Bright color represents higher values in IC coefficients. The ring-like spatial patterns around the ventricle are marked with red circles, showing this pattern loads heavily on voxels around structural boundary.

such effects. Uses of simpler less accurate registration methods would presumably be more susceptible to the effects of misregistration described here. The use of the FKT may be used to isolate changes in morphology from DTI changes.

## 4.5 Summary of contributions

We proposed a complementary method to assessing DTI data – namely that of examining common spatial patterns in FA or ADC using both the FKT and ICA. The use of ICA on FA and/or ADC values requires fewer and less stringent assumptions than tractography, but still requires that some conditions are met. It assumes that the data are perfectly registered (although this can be mitigated by utilizing the FKT and subspace selection outlined in this paper), and it assumes that the ADC/FA values in a given subject can be modelled as a linear superposition of spatially independent patterns. Because each voxel is treated independently with this approach, the emergent spatial patterns will be less likely affected by some of the situations which may cause difficulty for tractography algorithms, e.g. crossing fibres. We suggest that the combined FKT-ICA approach provides a novel way to assess DTI data in-between the simple approach of simply averaging values within a given region, and tractography which requires stringent assumptions.

# Chapter 5

# Conclusion

In this thesis we presented novel methods to analyze multi-modal brain image data such as MRI, SWI, DTI, and to extract brain morphometric features related to Parkinson's Disease. Our algorithms were tested on clinical data acquired from both PD subjects and age-matched normal control subjects. Our results demonstrate that inter-subject anatomical variability caused by misregistration is common after low-dimensional registration methods, and is often mis-interpreted to represent disease-related patterns in many voxel-based morphometry studies. High dimensional registration methods such as LDDMM can significantly improve the registration accuracy. However, these methods usually require large amounts of computation, and subtle residual misregistration still exists. To avoid mis-interpretation of anatomical variability, we proposed a deformation-based morphometry method that analyzed the initial momentum of deformation field, rather than the voxel values from the brain images directly. Compared to other morphometry methods, this method has the advantages of: 1) allowing joint analysis of a group of ROIs rather than single ROIs individually and 2) allowing analysis of local deformation patterns on the surfaces of ROIs to assess both atrophy and hypertrophy.

We demonstrated how use of the Fukunaga-Koontz Transform can be used to transform registered T1 and DTI images to a common space with complementary loadings so that linear subspaces emphasizing T1 variability or DTI variability can be selected. While we concentrated on T1 and DTI images, we note that the same approach can be applied to images of other modalities. In assessing the selected linear subspaces, we choose Independent Component Analysis as a decomposition method because 1) ICA can reduce the dimension of features from the number of voxels to the number of ICs, thus significantly reduces

the number of multiple compares in group difference tests; 2) ICs are of same dimension with the original images, which means they can be overlaid on a structural image directly and allow anatomical interpretation of the significant spatial patterns and 3) the higher correspondence between ICs loadings and clinical indices compared to other decomposition methods (such as PCA) implies that ICs have greater biological significance.

## 5.1 Future directions

1. Clinic interpretations of the PD-related patterns detected. In this thesis, we developed a brain morphometry method that can extract features that show significant correlation with subjects' clinical scores. The scores that we examined emphasized motor features. However, there may be other correspondences between the extracted morphological changes and cognitive aspects (e.g. memory). We note that the extracted features are in the same dimension of the original brain images, and therefore can be overlaid on a structural brain image, potentially allowing clinic experts to examine these patterns for biological interpretation.

2. Joint analysis of T1 and SWI image data using Fukunaga-Koontz transform. In Chapter 3 we have improved the registration of SWI maps by using multi-structure LDDMM algorithm. The next step would be to implement the FKT algorithms in Chapter 4 to extract the anatomical variability from registered SWI maps and use ICA to find PD-related ICs on the SWI-weighted linear subspace.

# Bibliography


[1] O. Abe, S. Aoki, N. Hayashi, H. Yamada, A. Kunimatsu, H. Mori, T. Yoshikawa, T. Okubo, and K. Ohtomo. Normal aging in the central nervous system: quantitative MR diffusion-tensor analysis. *Neurobiology of Aging*, 23:433–441, 2002.

[2] O. Almeida, E. Burton, I. McKeith, A. Gholkar, D. Burn, and J. O'Brien. MRI study of caudate nucleus volume in Parkinson's disease with and without dementia with Lewy bodies and Alzheimer's disease. *Dement Geriatr Cogn Disord*, 16:57–63, 2003.

[3] J. Andersson, C. Hutton, J. Ashburner, R. Turner, and K.J. Friston. Modelling geometric deformations in epi time series. *NeuroImage*, 13:903–919, 2001.

[4] C. Antoniades and R. Barker. The search for biomarkers in Parkinson's disease: a critical review. *Expert Review of Neurotherapeutics*, 8:1841–1852, 2008.

[5] L. G. Apostolova, M. Beyer, A. E. Green, K. S. Hwang, J. H. Morra, Y. Chou, and C. Avedissian. Hippocampal, caudate, and ventricular changes in Parkinson's disease with and without dementia. *Movement Disorders*, 25(6):687–695, 2010.

[6] J. Ashburner and K. J. Friston. Nonlinear spatial normalization using basis functions. *Hum. Brain Mapp.*, 7:254–266, 1999.

[7] A. Atkinson, W. Colburn, V. DeGruttola, D. DeMets, G. Downing, D. Hoth, J. Oates, C. Peck, R. Schooley, and B. Spilker. Biomarkers and surrogate endpoints: preferred definitions and conceptual framework. *Clinical Pharmacology and Therapeutics*, 69:89–95, 2001.

[8] M. F. Beg, Michael I. Miller, A. Trouve, and L. Younes. Computing large deformation metric mappings via geodesic flows of diffeomorphisms. *International Journal of Computer Vision*, 61:139–157, 2005.

[9] T. E. Behrens, H. Johansen-Berg, M. W. Woolrich, S. M. Smith, C. A. Wheeler-Kingshott, and P. A. Boulby. Non-invasive mapping of connections between human thalamus and cortex using diffusion imaging. *Nature Neuroscience*, 6:750–757, 2003.

[10] Y. Benjamini and Y. Hochberg. Controlling the false discovery rate: a practical and powerful approach to multiple testing. *Journal of the Royal Statistical Society, Series B (Methodological)*, 57 (1):289–300, 1995.

[11] D. Berg, B. Merz, K. Reiners, M. Naumann, and G. Becker. Five-year follow-up study of hyperechogenicity of the substantia nigra in Parkinson's disease. *Movement Disorders*, 20:383–384, 2005.

[12] L. Bergouignan, M. Chupin, Y. Czechowska, S. Kinkingnhun, C. Lemogne, G. Le Bastard, M. Lepage, and L. Garnero. Can voxel based morphometry, manual segmentation and automated segmentation equally detect hippocampal volume differences in acute depression? *Neuroimage*, 45:29–37, 2009.

[13] L. Bonilha, J. C. Edwards, S. L. Kinsman, P. S. Morgan, J. Fridriksson, C. Rorden, Z. Rumboldt, D. R. Roberts, M. A. Eckert, and J. J. Halford. Extrahippocampal gray matter loss and hippocampal deafferentation in patients with temporal lobe epilepsy. *Epilepsia*, 51:519, 2010.

[14] F. L. Bookstein. Voxel-based morphometry should not be used with imperfectly registered images. *Neuroimage*, 14:1454–1462, 2001.

[15] M. Bozzali, A. Falini, M. Franceschi, M. Cercignani, M. Zuffi, G. Scotti, G. Comi, and M. Filippi. White matter damage in Alzheimer's disease assessed in vivo using diffusion tensor magnetic resonance imaging. *J Neurol Neurosurg Psychiatry*, 72:742–746, 2002.

[16] C. Brenneis, K. Egger, C. Scherfler, K. Seppi, M. Schocke, W. Poewe, and G.K. Wenning. Progression of brain atrophy in multiple system atrophy. *Journal of Neurology*, 254:191–196, 2007.

[17] E. J. Burton, I. G. McKeith, D. J. Burn, and J. T. O'Brien. Brain atrophy rates in Parkinson's disease with and without dementia using serial magnetic resonance imaging. *Movement Disorders*, 20:1571–1576, 2005.

[18] E. J. Burton, I. G. McKeith, D. J. Burn, E. D. Williams, and J. T. OBrien. Cerebral atrophy in parkinsons disease with and without dementia: a comparison with Alzheimer's disease, dementia with Lewy bodies and controls. *Brain*, 127(4):791–800, 2004.

[19] V. D. Calhoun, T. Adali, N. R. Giuliani, J. J. Pekar, K.A. Kiehl, and G.D. Pearlson. Method for multimodal analysis of independent source differences in schizophrenia: combining gray matter structural and auditory oddball functional data. *Human Brain Mapping*, 27:47–62, 2006.

[20] D. Chan, J. C. Janssen, J. L. Whitwell, H. C.Watt, R. Jenkins, C. Frost, M. N. Rossor, and N. C. Fox. Change in rates of cerebral atrophy over time in early-onset Alzheimer's disease: longitudinal MRI study. *Lancet*, 362:1121–22, 2003.

[21] L. L. Chan, H. Rumpel, K. Yap, E. Lee, H. V. Loo, G. L. Ho, S. Fook-Chong adn Y. Yuen, and E. K. Tan. Case control study of diffusion tensor imaging in Parkinson's disease. *J Neurol Neurosurg Psychiatry*, 78:1383–6, 2007.

[22] J. Chen, A. R. Khan, M. J. McKeown, and M. F. Beg. Momentum-based morphometric analysis with application to Parkinson's disease. In *SPIE Symposium on Medical Imaging*, 2011.

[23] J. Chen, M. J. McKeown, and M. F. Beg. Variability of basal ganglia morphology after spatial normalization: Implications for group studies. In *33rd Conference of the Canadian Medical and Biological Engineering Society, Vancouver*, 2010.

[24] J. Chen, S. J. Palmer, A. R. Khan, M. J. McKeown, and M. F. Beg. Freesurfer-initialized large deformation diffeomorphic metric mapping with application to Parkinson's disease. In *SPIE Symposium on Medical Imaging*, 2009.

[25] A. Cherubini, P. Peran, C. Caltagirone, U. Sabatini, and G. Spalletta. Aging of subcortical nuclei: microstructural, mineralization and atrophy modifications measured in vivo using MRI. *Neuroimage*, 48:29–36, 2009.

[26] G. E. Christensen, S. C. Joshi, and M. I. Miller. Volumetric transformation of brain anatomy. *IEEE Transactions on Medical Imaging*, 16:864–77, 1997.

[27] G. E. Christensen, R. D. Rabbitt, and M. I. Miller. Deformable templates using large deformation kinematics. *IEEE Transactions on Image Processing*, 5(10):1435–47, 1996.

[28] T. C. Chua, W. Wen, X. Chen, N. Kochan, M. J. Slavin, J. N. Trollor, H. Brodaty, and P. S. Sachdev. Diffusion tensor imaging of the posterior cingulate is a useful biomarker of mild cognitive impairment. *American Journal of Geriatric Psych*, 17:602, 2009.

[29] M. Chupin, A. R. Mukuna-Bantumbakulu, D. Hasboun, E. Bardinet, S. Baillet, S. Kinkingn'ehun, L. Lemieux, B. Dubois, and L. Garnerob. Anatomically constrained region deformation for the automated segmentation of the hippocampus and the amygdala: method and validation on controls and patients with Alzheimer's disease. *Neuroimage*, 34:995–1019, 2007.

[30] A. Collignon, F. Maes, D. Delaere, D. Vandermeulen, P. Suetens, and G.Marchal. Automated multi-modality image registration based on information theory. In *Proc. Information Processing in Medical Imaging*, pages 263–274, 1995.

[31] D. L. Collins. *3D model-based segmentation of individual brain structures from magnetic resonance imaging.* PhD thesis, Mc Gill University, 1994.

[32] D. L. Collins, A. P. Zijdenbos, V. Kollokian, J. G. Sled, N. J. Kabani, C. J. Holmes, and A. C. Evans. Design and construction of a realistic digital brain phantom. *IEEE Transactions on Medical Imaging*, 17(3):463–468, June 1998.

[33] J. G. Csernansky, L.Wang, S. Joshi, J. P. Miller, M. Gado, D. Kido, D. McKeel, J. C. Morris, and M. I. Miller. Early DAT is distinguished from aging by high-dimensional mapping of the hippocampus. *Neurology*, 55:1636–1643, 2000.

[34] P. Damier, E. Hirsch, Y. Agid, and A. Graybiel. The substantia nigra of the human brain: patterns of loss of dopamine-containing neurons in Parkinson's disease. *Brain*, 122:1437–1448, 1999.

[35] C. Davatzikos. Why voxel-based morphometric analysis should be used with great caution when characterizing group differences. *Neuroimage*, 23:17–20, 2004.

[36] S. Duchesne, A. Caroli, C. Geroldi, C. Barillot, G. B. Frisoni, and D. L. Collins. MRI-based automated computer classification of probable AD versus normal controls. *IEEE Transactions on Medical Imaging*, 27:509–520, 2008.

[37] S. Duchesne, Y. Rolland, and M. Verin. Automated computer differential classification in Parkinsonian syndromes via pattern analysis on mri. *Academic Radiology*, 16:61–70, 2009.

[38] C. Eckart, C. Stoppel, J. Kaufmann, C. Tempelmann, H. Hinrichs, T. Elbert, H. J. Heinze, and I. T. Kolassa. Structural alterations in lateral prefrontal, parietal and posterior midline regions of men with chronic posttraumatic stress disorder. *Journal of Psychiatry and Neuroscience*, 36:176, 2011.

[39] M. A. Eckert, A. Tenforde, A. M. Galaburda, J. R. Korenberg U. Bellugi, D. Mills, and A. L. Reiss. To modulate or not to modulate: differing results in uniquely shaped Williams syndrome brains. *Neuroimage*, 32(3):1001–7, 2006.

[40] B. Fischl, D. H. Salat, E. Busa, M. Albert, M. Dieterich, C. Haselgrove, A. van der Kouwe, R. Killiany, D. Kennedy, S. Klaveness, A. Montillo, N. Makris, B. Rosen, and A. M. Dale. Whole brain segmentation: automated labeling of neuroanatomical structures in the human brain. *Neuron*, 33:341–355, 2002.

[41] P. A. Freeborough and N. C. Fox. MR image texture analysis applied to the diagnosis and tracking of Alzheimer's disease. *IEEE Transactions on Medical Imaging*, 17:475–479, 1998.

[42] G. B. Frisoni, F. Sabattoli, A. D. Lee, R. A. Dutton, A. W. Toga, and P. M. Thompson. In vivo neuropathology of the hippocampal formation in AD: a radial mapping MR-based study. *NeuroImage*, 32:104–110, 2006.

[43] G. B. Frisoni, C. Testa, A. Zorzan, F. Sabattoli, A. Beltramello, H. Soininen, and M. P. Laakso. Detection of grey matter loss in mild Alzheimer's disease with voxel based morphometry. *Journal of Neurology and Neurosurgery and Psychiatry*, 73:657–664, 2002.

[44] F. Fukunaga and W. Koontz. Applications of the karhunen-loeve expansion to feature selection and ordering. *IEEE Transactions on Computers*, 19 (5):311–318, 1970.

[45] G. Gattellaro, L. Minati, M. Grisoli, C. Mariani, F. Carella, and M. Osio. White matter involvement in idiopathic Parkinson disease: a diffusion tensor imaging study. *AJNR Am J Neuroradiol*, 30:1222–6, 2009.

[46] D. Geng, Y. Li, and C. Zee. Magnetic resonance imaging-based volumetric analysis of basal ganglia nuclei and substantia nigra in patients with Parkinson's disease. *Neurosurgery*, 58:256, 2006.

[47] M. Ghaemi, R. Hilker, J. Rudolf, J. Sobesky, and W. Heiss. Differentiating multiple system atrophy from Parkinson's disease: contribution of striatal and midbrain MRI volumetry and multi-tracer PET imaging. *Journal of Neurology, Neurosurgery and Psychiatry*, 73:517–523, 2002.

[48] S. Gouttard, M. Styner, S. Joshi, R. G. Smith, H. C. Hazlett, and G. Gerig. Subcortical structure segmentation using probabilistic atlas priors. In *SPIE*, 2007.

[49] U. Grenander and M. I. Miller. Computational anatomy: an emerging discipline. *Quarterly of Applied Mathematics*, LVI:617–694, 1998.

[50] J. Henderson, K. Carpenter, H. Cartwright, and G. Halliday. Degeneration of the centre median-parafascicular complex in Parkinson's disease. *Annals of Neurology*, 47:345–352, 2000.

[51] J. Himberg, A. Hyvarinen, and F. Esposito. Validating the independent components of neuroimaging time-series via clustering and visualization. *NeuroImage*, 22:1214–1222, 2004.

[52] I. Hollinger, A. Geissler, M. Wurnig, S. Gruber, J. Rath, S. Robinson, S. Trattnig, and R. Beisteiner. Influence of skull stripping on functional MRI data. In *16th Annual Meeting of the Organization for Human Brain Mapping*, 2010.

[53] C. J. Holmes, R. Hoge, L. Collins, R. Woods, A. W. Toga, and A. C. Evans. Enhancement of MR images using registration for signal averaging. *Journal of Computer Assisted Tomography*, 22(2):324–333, 1998.

[54] A. Hood, S. Amador, A. Cain, K. Briand A. Al-Refai, M. Schiess, and A. Sereno. Levodopa slows prosaccades and improves antisaccades: an eye movement study in Parkinson's disease. *British Medical Journal*, 78:565, 2007.

[55] X. Huang, Y. Z. Lee, M. McKeown, G. Gerig, H. Gu, W. Lin, M. M. Lewis, S. Ford, A. I. Trester, and D. R. Weinberger. Asymmetrical ventricular enlargement in Parkinson's disease. *Movement Disorders*, 22:1657–1660, 2007.

[56] X. Huo. A statistical analysis of Fukunaga-Koontz transform. *IEEE Signal Processing Letters*, 11(2):123–126, 2004.

[57] N. Ibarretxe-Bilbao, C. Junque, M. J. Marti, F. Valldeoriola, P. Vendrell, and N. Bargallo. Olfactory impairment in Parkinson's disease and white matter abnormalities in central olfactory areas: a voxel-based diffusion tensor imaging study. *Movement Disorders*, 25:1888–94, 2010.

[58] J. Kassubek, F. D. Juengling, B. Hellwig, J. Spreer, and C. H. Lucking. Thalamic gray matter changes in unilateral Parkinsonian resting tremor: a voxel-based morphometric analysis of 3-dimensional magnetic resonance imaging. *Neurosci Lett.*, 323(1):29–32, 2002.

[59] A. T. Karagulle Kendi, S. Lehericy, M. Luciana, K. Ugurbil, and P. Tuite. Altered diffusion in the frontal lobe in Parkinson disease. *AJNR Am J Neuroradiol*, 29:501–5, 2008.

[60] A. R. Khan. *Improving brain registration and segmentation using anatomical guidance.* PhD thesis, Simon Fraser University, 2011.

[61] A. R. Khan and M. F. Beg. Multi-structure whole brain registration and population average. In *IEEE Engineering in Medicine and Biology Society Conference*, 2009.

[62] A. R. Khan, L. W., and M. F. Beg. Freesurfer-initiated fully-automated subcortical brain segmentation in MRI using large deformation diffeomorphic metric mapping. *NeuroImage*, 41(3):735–46, 2008.

[63] A. Klein and J. Hirsch. Mindboggle: a scatterbrained approach to automate brain labeling. *NeuroImage*, 24:261–280, 2005.

[64] K. Krabbe, M. Karlsborg, A. Hansen, L. Werdelin, J. Mehlsen, H. Larsson, and O. Paulson. Increased intracranial volume in Parkinson's disease. *Journal of the Neurological Sciences*, 239:45–52, 2005.

[65] B. A. Landman, J. A. D. Farrell, N. L. Patela, S. Mori, and J. L. Prince. Dti fiber tracking: the importance of adjusting DTI gradient tables for motion correction. In *Human Brain Mapping*, 2007.

[66] E. L. Lehmann. *Testing statistical hypotheses.* Wiley, New York, 1986.

[67] J. P. Lerch, J. C. Pruessner, A. Zijdenbos, H. Hampel, S. J. Teipel, and A. C. Evans. Focal decline of cortical thickness in Alzheimer's disease identified by computational neuroanatomy. *Cereb Cortex*, 15:995–1001, 2005.

[68] M. M. Lewis, A. B. Smith, M. Styner, H. Gu, R. Poole, H. Zhu, Y. Li, X. Barbero, S. Gouttard, M. J. McKeown, R. B. Mailman, and X. Huang. Asymmetrical lateral ventricular enlargement in Parkinson's disease. *Eur J Neurol*, 16:475–481, 2009.

[69] W. Li, J. Liu, F. Skidmore, Y. Liu, J. Tian, and K. Li. White matter microstructure changes in the thalamus in Parkinson disease with depression: a diffusion tensor MR imaging study. *AJNR Am J Neuroradiol*, 31:1861–6, 2010.

[70] S. Lisanby, W. McDonald, E. Massey, P. Doraiswamy, M. Rozear, O. Boyko, K. Krishnan, and C. Nemeroff. Diminished subcortical nuclei volumes in Parkinson's disease by MR imaging. *Journal of Neural Transmission-Supplement*, 40:13–21, 1993.

[71] W. W. R. Martin, M. Wieler, and M. Gee. Midbrain iron content in early Parkinson disease: a potential biomarker of disease status. *Neurology*, 70(2):1411–1417, 2008.

[72] M. J. McKeown, A. Uthama, R. Abugharbieh, S. Palmer, M. Lewis, and X. Huang. Shape (but not volume) changes in the thalami in Parkinson disease. *BMC Neurology*, 8:8, 2008.

[73] M. I. Miller, A. Trouve, and L. Younes. Geodesic shooting for computational anatomy. *Journal of Mathematical Imaging and Vision*, 24:209–228, 2006.

[74] A. Nagano-Saito, Y. Washimi, Y. Arahata, T. Kachi, J. Lerch, A. Evans, A. Dagher, and K. Ito. Cerebral atrophy and its relation to cognitive impairment in Parkinson disease. *Neurology*, 64:224, 2005.

[75] A. Nagano-Saito, Y. Washimi, Y. Arahata, T. Kachi, J. P. Lerch, A. C. Evans, A. Dagher, and K. Ito. Cerebral atrophy and its relation to cognitive impairment in Parkinson disease. *Neurology*, 64:224–229, 2005.

[76] J. Neumann, G. Lohmann, J. Derrfuss, and D. Y. von Cramon. Meta-analysis of functional imaging data using replicator dynamics. In *Human Brain Mapping*, 2005.

[77] A. Nieto-Castanon, S. S. Ghosh, J. A. Tourville, and F. H. Guenther. Region of interest based analysis of functional imaging data. *NeuroImage*, 19(4):1303–16, 2003.

[78] D. Ostwald, C. Porcaro, and A. P. Bagshaw. An information theoretic approach to EEG-fMRI integration of visually evoked responses. *NeuroImage*, 49:498–516, 2010.

[79] D. C. Paviour, S. L. Price, M. Jahanshahi, A. J. Lees, and N.C. Fox. Longitudinal MRI in progressive supranuclear palsy and multiple system atrophy: rates and regions of atrophy. *Brain*, 129:1040, 2006.

[80] A. Pitiot., H. Delingettea, P. M. Thompson, and N. Ayachea. Expert knowledge-guided segmentation system for brain MRI. *NeuroImage*, 23 Supplement 1:S85–S96, 2004.

[81] H. Pol, W. van der Flier, H. Schnack, C. Tulleken, L. Ramos, J. van Ree, and R. Kahn. Frontal lobe damage and thalamic volume changes. *Neuroreport*, 11:3039, 2000.

[82] T. Rohlfing, R. Brandtb, R. Menzelb, and C. R. Maurer Jr. Evaluation of atlas selection strategies for atlas-based image segmentation with application to confocal microscopy images of bee brains. *NeuroImage*, 21:1428–1442, 2004.

[83] C. Rorden and M. Brett. Stereotaxic display of brain lesions. *Behav Neurol*, 12(4):191–200, 2000.

[84] C. S. Roy and C. S. Sherrington. On the regulation of the blood-supply of the brain. *Journal of Physiology*, 11:85–158, 1890.

[85] L. Rui, J. L. Krolik, and M. J. McKeown. An information-theoretic criterion for intra-subject alignment of fMRI time-series: motion corrected independent component analysis. *Medical Imaging and IEEE Transactions on*, 24(1):29–44, 2005.

[86] C. Scherfler, M. F. Schocke, K. Seppi, R. Esterhammer, C. Brenneis, W. Jaschke, G. K. Wenning, and W. Poewe. Voxel-wise analysis of diffusion weighted imaging reveals disruption of the olfactory tract in Parkinson's disease. *Brain*, 129:538–542, 2006.

[87] J. Schulz, M. Skalej, D. Wedekind, A. Luft, M. Abele, K. Voigt, J. Dichgans, and T. Klockgether. Magnetic resonance imaging-based volumetry differentiates idiopathic parkinson's syndrome from multiple system atrophy and progressive supranuclear palsy. *Annals of Neurology*, 45:65–74, 1999.

[88] D. Shen and C. Davatzikos. Hammer: hierarchical attribute matching mechanism for elastic registration. *IEEE Transactions on Medical Imaging*, 21(11):1421–1439, 2002.

[89] Y. Song, F. Nie, C. Zhang, and S. Xiang. A unified framework for semi-supervised dimensionality reduction. *Pattern Recognition*, 41:2789–2799, 2008.

[90] I. Steiner, J. Gomori, and E. Melamed. Features of brain atrophy in Parkinson's disease. *Neuroradiology*, 27:158–160, 1985.

[91] M. Stern. The preclinical detection of Parkinson's disease: ready for prime time? *Annals of Neurology*, 56:169–170, 2004.

[92] H. Stockner, M. K. K. Sojer, J. Mueller, G. Wenning, C. Schmidauer, and W. Poewe. Midbrain sonography in patients with essential tremor. *Movement Disorders*, 22:414–416, 2007.

[93] C. Studholme, D. L. G. Hill, and D. J. Hawkes. An overlap invariant entropy measure of 3D medical image alignment. *Pattern Recognition*, 32:71–86, 1999.

[94] J. Talairach and P. Tournoux. *Co-planar stereotaxic atlas of the human brain: 3-dimensional proportional system - an approach to cerebral imaging.* Thieme Medical Publishers, 1988.

[95] P. M. Thompson, K. M. Hayashi, G. de Zubicaray, A. L. Janke, S. E. Rose, J. Semple, D. Herman, M. S. Hong, S. S. Dittmer, D. M. Doddrell, and A. W. Toga. Dynamics of gray matter loss in Alzheimer's disease. *The Journal of Neuroscience*, 23:994–1005, 2003.

[96] P. M. Thompson, K. M. Hayashi, G. I. De Zubicaray, A. L. Janke, S. E. Rose, J. Semple, M. S. Hong, D. H. Herman, D. Gravano, D. M. Doddrell, and A. W. Toga.

Mapping hippocampal and ventricular change in Alzheimer disease. *NeuroImage*, 22:1754–1766, 2004.

[97] L. C. Tzarouchi, L.G. Astrakas, S. Konitsiotis, S. Tsouli, P. Margariti, A. Zikou, and M.I. Argyropoulou. Voxel based morphometry and voxel based relaxometry in Parkinsonian variant of multiple system atrophy. *Journal of Neuroimaging*, 20:260–266, 2010.

[98] N. Tzourio-Mazoyer, B. Landeau, D. Papathanassiou, F. Crivello, O. Etard, N. Delcroix, B. Mazoyer, and M. Joliot. Automated anatomical labeling of activations in spm using a macroscopic anatomical parcellation of the MNI MRI single subject brain. *NeuroImage*, 15(1):273–89, 2002.

[99] D. Vaillancourt, M. Spraker, J. Prodoehl, I. Abraham, D. Corcos, X. Zhou, C. Comella, and D. Little. High-resolution diffusion tensor imaging in the substantia nigra of de novo Parkinson disease. *Neurology*, 72:1378, 2009.

[100] P. Valkovic, S. Krafczyk, M. Saling, J. Benetin, and K. Botzel. Postural reactions to neck vibration in Parkinson's disease. *Movement Disorders*, 21:59–65, 2006.

[101] L. Wang, M. F. Beg, T. Ratnanather, C. Ceritoglu, L. Younes, J. C. Morris, and J. G. Csernanskyand M. I. Miller. Large deformation diffeomorphism and momentum based hippocampal shape discrimination in dementia of the Alzheimer type. *Medical Imaging and IEEE Transactions on*, 26(4):462–470, 2007.

[102] W. M. Wells, P. Viola, H. Atsumi, S. Nakajima, and R. Kikinis. Multi-modal volume registration by maximisation of mutual information. *Medical Image Analysis*, 1:35–51, 1996.

[103] Y. Xia, K. Bettinger, L. Shen, and A. L. Reiss. Automatic segmentation of the caudate nucleus from human brain MR images. *Medical Imaging and IEEE Transactions on*, 26(4):509–517, April 2007.

[104] K. Yoshikawa, Y. Nakata, K. Yamada, and M. Nakagawa. Early pathological changes in the Parkinsonian brain demonstrated by diffusion tensor MRI. *Journal of Neurology and Neurosurgery and Psychiatry*, 75:481, 2004.

[105] M. J. Zigmond, E. D. Abercrombie, T. W. Berger, A. A. Grace, and E. M. Stricker. Compensatory responses to partial loss of dopaminergic neurons: studies with 6-hydroxydopamine. In *In Current Concepts in Parkinson's Disease Research*, pages 99–140, 1993.

# Appendix A

# Automated fMRI Signal Processing Tool: fPipe

## A.1 Introduction

Functional magnetic resonance imaging is a specialized MRI method. In fMRI data, the contast of blood-oxygen-level dependence (BOLD) is used to measure the changes in blood flow and blood oxygenation in the brain, which are both closely related to neural activity [84].

The traditional fMRI study usually involves extracting the voxel values (i.e. BOLD signals) within certain ROI over time, known as time courses. The study usually contains a combined procedure including slicing timing correction, motion correction, structural segmentation, spatial normalization, time course extraction and statistical analysis. These user-defined procedures usually involves more than one tools such as SPM, Amira and MRICro. Using multiple software reduced the efficiency of data processing and organization, as these each software has its own protocol of file naming and parameter set up. Misunderstanding happens when different researchers working on the same data pass around middle results. To improved the efficiency and reduce the manual labor for the users, we developed a Matlab toolbox "fPipe" that can automatically run the whole customer defined procedure one step after another, with all the steps configured within one graphic user interface. The middle results are stored in unified formats, so that the procedure can easily be re-run from any step given results of one step before.

## A.2 Previous methods

The routine fMRI processing method involves user interaction with several different software. The middle results are named and stored manually. The extraction and analysis of time courses from fMRI data usually contains the following steps.

### A.2.1 Pre-processing with Brain Voyager

Raw data are in Philips PAR format. Each subject has a head file (.par) with scanning parameters and an actual data file (.rec). Brain Voyager was used to create a .fmr file that contains the parameters of the functional data set and links to a single .stc file for each slice. For the first-time analysis subjects pre-processing including 3D motion correction and slicing timing correction were also applied. The pre-processed data were then exported as image files of Analyze 7.5 format.

### A.2.2 Skull stripping with BET

For all scans (structural and functional), the skull was removed using the Brain Extraction Tool (BET), which is implemented in the software MRICro. For more details refer to "www.fmrib.ox.ac.ukfsl". Prefix "SS_" was added automatically to the skull-stripped image files.

### A.2.3 Co-registration and segmentation with Amira

Amira is used to co-register the anatomical and functional scans, and to draw the ROIs on each brain. There are 3 scripts that are used for this purpose: pre-segmentation.scro, postsegmentation.scro, and alreadysegmented.scro. These can be found in the AmiraTest folder on Petshare.

At this stage for each participant there should be a set of functional scans in Analyze format which are all aligned to the first volume of the first functional run. For patients who are scanned off and on med, the scans will be aligned to the first functional volume of each session. There should also be a skull-stripped anatomical scan in Analyze format and a skull-stripped version of the first volume of every run.

We typically draw 9 ROIs in each hemisphere. The hemisphere visible on the left side of the screen is the RIGHT hemisphere. ROIs were drawn in the following order and labeled

as follows:

- Right putamen R_PUT
- Left putamen L_PUT
- Right caudate R_CAU
- Left caudate L_CAU
- Right globus pallidus R_GLP
- Left globus pallidus L_GLP
- Right thalamus R_THA
- Left thalamus L_THA
- Right cerebellum R_CER
- Left cerebellum L_CER
- Right primary motor cortex R_M1
- Left primary motor cortex L_M1
- Right supplementary motor area R_SMA
- Left supplementary motor area L_SMA
- Right anterior cingulate cortex R_ACC
- Left anterior cingulate cortex L_ACC
- Right prefrontal cortex R_PFC
- Left prefrontal cortex L_PFC

### A.2.4 Time course analysis with Matlab

Finally the time courses were extracted using manually drawn ROIs as masks. Any analysis after this was conducted in Matlab.

## A.3 Proposed methods

We developed a Matlab toolbox called fPipe. It has all the functions of routine method. It also has the following features:

- Single platform: All the tasks are now completed under Matlab, which can be run from both Windows and Linux system. Middle results are stored with uniformed file names and folder structures.
- Fully automated: Once the parameters are set, all the tasks can be performed in sequence without any user interaction.
- User friendly: Graphic User Interface (GUI) is available for parameters setup.
- Modulated sub-functions: like the traditional method, the whole procedure consists of a series of tasks. We made each task into an independent module, so that the user can start from, skip, or re-run any of these modules easily with the GUI shown in Figure A.2.

The workflow of the whole fPipe is shown in Figure A.1.

### A.3.1 Raw data import

The purpose of this module is to covert raw data from Philips PARREC format into Analyze 7.5 format for initial visualization and pre-processing. We implemented a Philips PARREC reader (Bennett Landman, 2005) to import both structural and functional raw data into Matlab. The fMRI images were then saved as a group of separated file in Analyze 7.5 format, each file corresponding to one time point.

### A.3.2 Slicing timing correction

The purpose of this module is to correct the time difference among slices of the same time point. During fMRI scan, slices of the brain volume are usually acquired one after another, therefore there is a time difference between slices. However, a single fMRI brain volume is usually treated as a time point, therefore temporal interpolation is needed to compute the slices at same time point. In fPipe we implemented the slicing time correction module of SPM to complete this step.

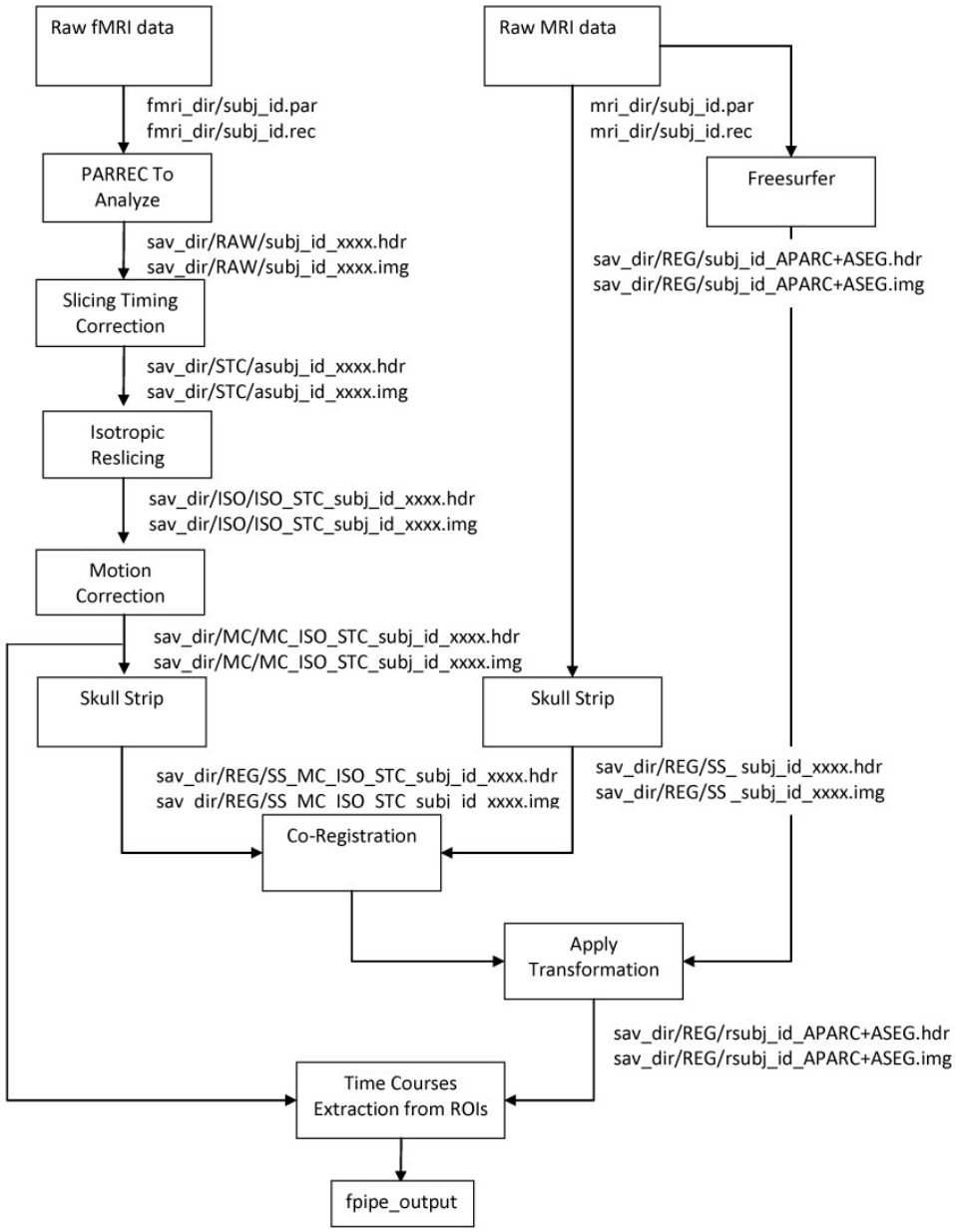


Figure A.1: The workflow of fMRI data processing in fPipe.

### A.3.3 Isotropic reslicing

The purpose of this module is to make the voxel size isotropic in all three dimension. For fMRI scans the number of slices is usually smaller than the length or width (also in voxel numbers) of each slice, making the voxel "'longer"' in the scanning direction. Spacial interpolation is needed to reslice the brain volume so that the voxels have cubic sizes. This will improve accuracy in the later co-registration. In fPipe we implemented an in-house developed Matalb function (Martin McKeown, 2004) to complete this task.

### A.3.4 Motion correction

The purpose of this module is to correct the shift of brain on fMRI images cause by the head movement of subjects during fMRI scan. In fPipe we used a combination of SPM Realign module [3] and MCICA algorithm [85] to complete this task.

### A.3.5 Skull strip

The purpose of this module is to remove the skull on structural image. In the traditional method skull strip was believed to improve the co-registration between structural and functional images. However, recent study [52] showed that skull stripping may reduce accuracy of co-registration, which was confirmed during our tests with fPipe. Therefore this step is skipped by default in fPipe. However, the module still exists and can be added to the procedure by user.

### A.3.6 Structural image segmentation

The purpose of this module is to perform automated segmentation on structural images, which can be used as masks in time course extraction module. In fPipe, we use a combined method of Freesurfer [40] and FS+LDDMM [62] for structural image segmentation.

FS+LDDMM method is a segmentation-by-registration method. The method contains the following steps.

First, FreeSurfer establishes initial labels of the target structures, which mainly contains five stages: an affine registration with Talairach space, an initial volumetric labeling, bias field correction, non-linear alignment to the Talairach space, and a final labeling of the volume.

Second, based on the FS labels, regions of interest (ROI) containing all target structures, linearly aligned, are cropped from the original images, to reduce the computational intensity and avoid trapping in local minima during LDDMM.

At last, LDDMM computes the deformation from the ROI of template image to ROI of each target image, then uses that deformation to map the manual labels, on template image, to automatic labels (i.e. segmentations) on target images. The LDDMM optimization uses a three stage procedure, starting with Cerebrospinal Fluid (CSF) labels (i.e. the portion of the ventricles in ROI), followed by Gaussian smoothed ROIs, and finally the original ROIs. Each step initializes with the optimal map computed at the previous stage, to avoid potential local minima.

We used FS+LDDMM for subcortical ROIs segmentation, and Freesurfer for cortical ROIs (including Brodmann areas) segmentation.

### A.3.7 Co-registration

The purpose of this module is to reslice the structural image into the same resolution as the functional image of that same subject, and to align the segmentations of ROIs on structural images with the functional images. We implemented the spacial normalization module in SPM to complete this task, with normalized mutual-information as cost function. The fMRI image used in the co-registration is the first time point of the reference points for the motion correction.

### A.3.8 Time course extraction

The purpose of this module is to co-register structural ROIs to fMRI image as mask and extract the fMRI time courses. The structural ROIs were generated with FS-LDDMM. The same transformations computed from the co-registration step were applied on the structural ROIs to propagate functional ROIs. The fMRI signals were then masked by these ROIs and saved separately.

### A.3.9 Output

The output of fPipe is a structure variable with following fields:

ROI - ROI name

label_value - label value in lookup table

pointer - index of non-zero voxels in the mask

hdr - analyze image info for restoration purpose

data - 2D matrix, each row is a time point of masked functional data

### A.3.10 Graphic user interface (GUI)

The GUI of fPipe is shown in Figure A.2. The user can choose structural and functional images and corresponding ROIs from the GUI, as well as decide which step to run the pipeline from and which ROIs to extract time courses for.

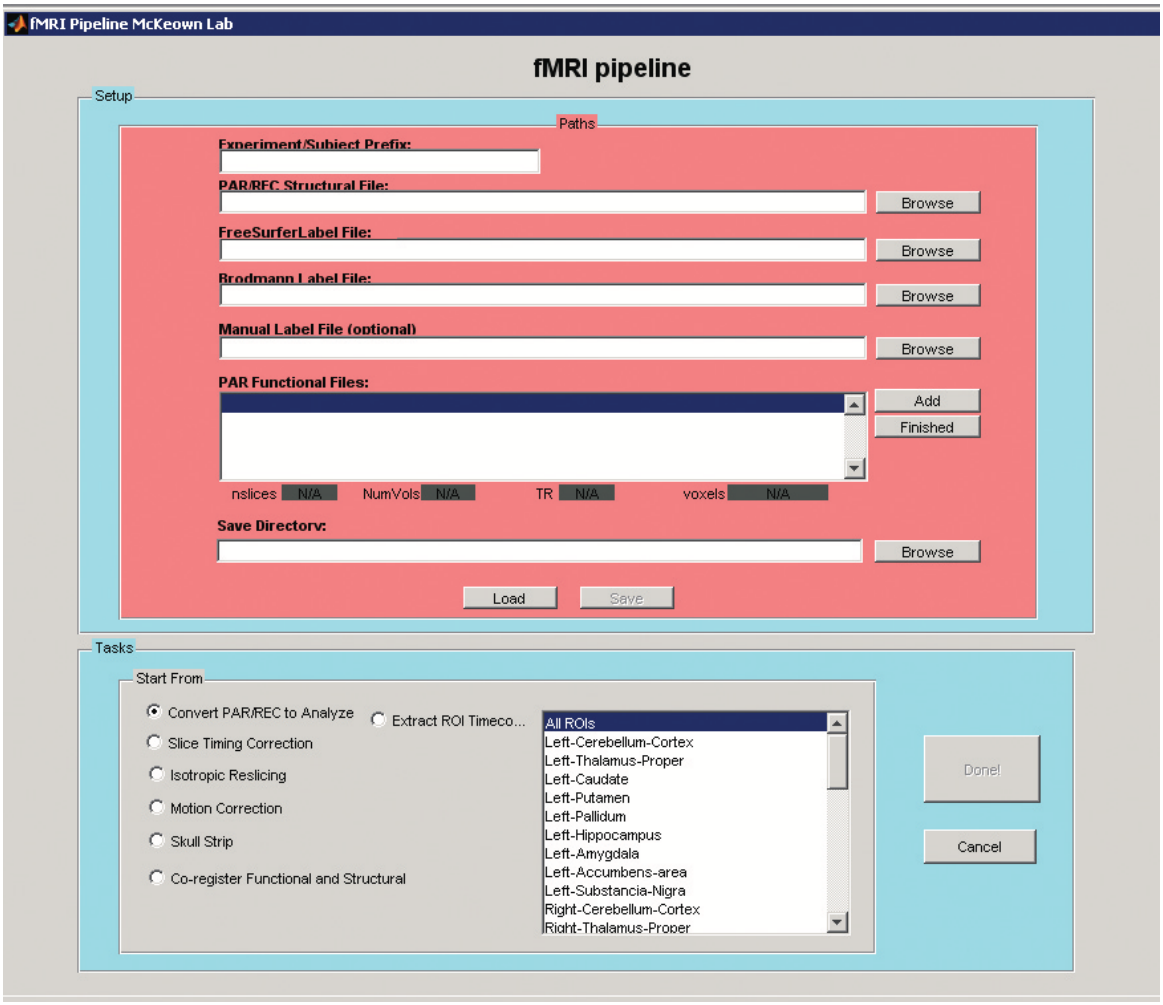


Figure A.2: GUI of fPipe.

## A.4 Running on cluster server

### A.4.1 Automation assumptions

Several assumptions are currently being made by the automation script (fpipecluster) which users must be aware of. The assumptions are:

- User can generate the parms.matfile locally on their own Matlab instance and also create a text (ASCII) version of that file for fpipeclusterto parse.
- Input data must be placed located on "meddata" folder, a network drive, so that fpipecluster can automatically copy data to scratch disk for processing.
- The "parms" files must be located on "meddata" folder so that fpipecluster on discovery server can be run using them as input.
- Users must have software ssh installed and login to cluster using a central "fmri" account and launch single command: fpipecluster (with appropriate arguments).
- On the computer where the "parms" file is generated, "meddata" folder must be mapped to X: and Xfer must be mapped to Z:. If this is not the case, fpipeclusterwill fail.
- The binary (.mat) and text (.txt) versions of the parms files must be located in the same directory and must be named identically except for the extensions which must be .matand .txt. Logging in to Discovery

All authorized fMRI users who require cluster access to run jobs are allowed to login to the cluster. The current login model is a single account for all fMRI users, named "fmri".

All access to discovery is done remotely with SSH. Users will require an SSH client on their computer to access the cluster. Currently, there is no direct external access to the cluster. To access the cluster remotely from the "outside world" (that is, while you're not on the PETfMRI network) you must first login to your respective external login host.

For fMRI, this host is wernicke.fmri.ubc.ca. Direct login from Windows workstations on the PET/fMRI network is allowed.

For Microsoft Windows systems, a popular free SSH client is putty. For Linux or Mac OS X, an SSH client is available by default. Windows users may also use the SSH client from "www.ssh.com".

### A.4.2 Using fpipecluster

The following usage information is displayed if fpipeclusters is called incorrectly or the "-h" flag is used:

```
usage: fpipecluster <-p parms.txt> [-s StartFrom] [-e email] [-h]

<-p parms.txt> Required, ASCII text version of parms.mat
[-s StartFrom] Optional, where to start processing
[-e email] Optional, for job notification emails
[-h] Help, display this message
```

For general use, the only important argument is "-p". This argument tells fpipecluster where to find the text (ASCII) version of the parms file for a specific job. It is the only required argument. The "-e" argument can be used to specify an email address where you would like the cluster to contact you when the job ends (either through failure or completion). This argument is not required and you may omit it if you do not desired to be notified.